

RESEARCH ARTICLE

10.1002/2014JE004681

Special Section:

Results from the first 360 Sols of the Mars Science Laboratory Mission: Bradbury Landing through Yellowknife Bay

Key Points:

- Fluvial sandstones analyzed by ChemCam display subtle chemical variations
- Combined analysis of chemistry and texture highlights the role of diagenesis
- Distinct chemistry in upper layers suggests distinct setting and/or source

Correspondence to:

N. Mangold,
nicolas.mangold@univ-nantes.fr

Citation:

Mangold, N., et al. (2015), Chemical variations in Yellowknife Bay formation sedimentary rocks analyzed by ChemCam on board the Curiosity rover on Mars, *J. Geophys. Res. Planets*, 120, 452–482, doi:10.1002/2014JE004681.

Received 20 JUN 2014

Accepted 3 FEB 2015

Accepted article online 6 FEB 2015

Published online 19 MAR 2015

Chemical variations in Yellowknife Bay formation sedimentary rocks analyzed by ChemCam on board the Curiosity rover on Mars

N. Mangold¹, O. Forni², G. Dromart³, K. Stack⁴, R. C. Wiens⁵, O. Gasnault², D. Y. Sumner⁶, M. Nachon¹, P.-Y. Meslin², R. B. Anderson⁷, B. Barraclough⁴, J. F. Bell III⁸, G. Berger², D. L. Blaney⁹, J. C. Bridges¹⁰, F. Calef⁹, B. Clark¹¹, S. M. Clegg⁵, A. Cousin⁵, L. Edgar⁸, K. Edgett¹², B. Ehlmann⁴, C. Fabre¹³, M. Fisk¹⁴, J. Grotzinger⁴, S. Gupta¹⁵, K. E. Herkenhoff⁷, J. Hurowitz¹⁶, J. R. Johnson¹⁷, L. C. Kah¹⁸, N. Lanza¹⁹, J. Lasue², S. Le Mouélic¹, R. Lévillé²⁰, E. Lewin²¹, M. Malin¹², S. McLennan¹⁶, S. Maurice², N. Melikechi²², A. Mezzacappa²², R. Milliken²³, H. Newsom¹⁹, A. Ollila¹⁹, S. K. Rowland²⁴, V. Sautter²⁵, M. Schmidt²⁶, S. Schröder², C. d'Uston², D. Vaniman²⁷, and R. Williams²⁷

¹Laboratoire de Planétologie et Géodynamique de Nantes, CNRS, Université de Nantes, Nantes, France, ²Institut de Recherche en Astrophysique et Planétologie, CNRS/Université de Toulouse, UPS-OMP, Toulouse, France, ³Laboratoire de Géologie de Lyon, Université de Lyon, Lyon, France, ⁴California Institute of Technology, Pasadena, California, USA, ⁵Los Alamos National Laboratory, Los Alamos, New Mexico, USA, ⁶Earth and Planetary Sciences, University of California, Davis, California, USA, ⁷Astrogeology Science Center, U.S. Geological Survey, Flagstaff, Arizona, USA, ⁸School of Earth and Space Exploration, Arizona State University, Tempe, Arizona, USA, ⁹Jet Propulsion Laboratory, California Institute of Technology, Pasadena, California, USA, ¹⁰Space Research Centre, Department of Physics and Astronomy, University of Leicester, Leicester, UK, ¹¹Space Science Institute, Boulder, Colorado, USA, ¹²Malin Space Science Systems, San Diego, California, USA, ¹³GéoRessources, Université de Lorraine, Nancy, France, ¹⁴Earth, Ocean and Atmospheric Science, Oregon State University, Corvallis, Oregon, USA, ¹⁵Department of Earth Science and Engineering, Imperial College London, London, UK, ¹⁶Department of Geosciences, State University of New York at Stony Brook, Stony Brook, New York, USA, ¹⁷Applied Physics Laboratory, Johns Hopkins University, Laurel, Maryland, USA, ¹⁸Department of Earth and Planetary Sciences, University of Tennessee, Knoxville, TN, USA, ¹⁹Department of Earth and Planetary Sciences, Institute of Meteoritics, Albuquerque, New Mexico, USA, ²⁰Canadian Space Agency, Saint-Hubert, Quebec, Canada, ²¹ISTerre, Université Joseph Fourier, Grenoble, France, ²²Applied Optics Center, Delaware State University, Dover, Delaware, USA, ²³Department of Geological Sciences, Brown University, Providence, Rhode Island, USA, ²⁴Department of Geology and Geophysics, University of Hawaii at Manoa, Honolulu, Hawaii, USA, ²⁵Museum National d'Histoire Naturelle de Paris, Paris, France, ²⁶Department of Earth Sciences, Brock University, St. Catharines, Ontario, Canada, ²⁷Planetary Science Institute, Tucson, Arizona, USA

Abstract The Yellowknife Bay formation represents a ~5 m thick stratigraphic section of lithified fluvial and lacustrine sediments analyzed by the Curiosity rover in Gale crater, Mars. Previous works have mainly focused on the mudstones that were drilled by the rover at two locations. The present study focuses on the sedimentary rocks stratigraphically above the mudstones by studying their chemical variations in parallel with rock textures. Results show that differences in composition correlate with textures and both manifest subtle but significant variations through the stratigraphic column. Though the chemistry of the sediments does not vary much in the lower part of the stratigraphy, the variations in alkali elements indicate variations in the source material and/or physical sorting, as shown by the identification of alkali feldspars. The sandstones contain similar relative proportions of hydrogen to the mudstones below, suggesting the presence of hydrous minerals that may have contributed to their cementation. Slight variations in magnesium correlate with changes in textures suggesting that diagenesis through cementation and dissolution modified the initial rock composition and texture simultaneously. The upper part of the stratigraphy (~1 m thick) displays rocks with different compositions suggesting a strong change in the depositional system. The presence of float rocks with similar compositions found along the rover traverse suggests that some of these outcrops extend further away in the nearby hummocky plains.

1. Introduction

The Mars Science Laboratory (MSL) rover, Curiosity, arrived at Gale crater in August 2012. The landing ellipse was chosen because of its proximity to Aeolis Mons (known informally as Mount Sharp), the central, 5 km high-layered mound within Gale crater. The layers comprising the mound are the prime target of the Curiosity mission. The area within the ellipse is also of interest because it is downslope from Peace Vallis

[Anderson and Bell, 2010, Palucis et al., 2014], a prominent gully cutting the inner wall of Gale crater. From the time of its landing at the Bradbury site until sol 53, the Curiosity rover traversed a clast-strewn terrain with local exposures of conglomerates [Williams et al., 2013]. On sol 53 Curiosity encountered a change in terrain to one with more in-place rock outcrops. The latter corresponds to a ~5 m thick assemblage of sedimentary rocks informally named Yellowknife Bay formation [Grotzinger et al., 2014].

Based on orbital mapping of High Resolution Imaging Science Experiment (HiRISE) images and in situ observations, the Yellowknife Bay formation was split from base to top into the Sheepbed, Gillespie Lake, and Glenelg members [Grotzinger et al., 2014]. At Sheepbed, two locations (John Klein and Cumberland) were drilled into a mudstone. The mineralogy of this mudstone was determined by the Chemistry and Mineralogy instrument (CheMin) instrument using X-ray diffraction [Vaniman et al., 2014]. The crystalline part of both samples is dominated by igneous minerals and two main secondary phases: calcium sulfates and smectite clays [Vaniman et al., 2014]. A large number of diagenetic features, including concretions, veins, sedimentary dikes and vugs, indicate a complex postdepositional evolution [Grotzinger et al., 2014]. Chemical analyses suggested that postdepositional aqueous alteration took place at combined water/rock ratios and pH levels that were modest enough such as mineralogical changes occurred under nearly isochemical conditions [McLennan et al., 2014]. The detailed analysis of the lacustrine mudstone indicated that this environment would have been readily habitable, with the potential for preserving biological markers, if life had existed in it [Grotzinger et al., 2014]. These fluvio-lacustrine sediments are likely connected with the Peace Vallis alluvial fan that formed after Gale crater formed (3.6 Gy ago) [Le Deit et al., 2013] in the Hesperian or Early Amazonian periods [Grant et al., 2014]. Many lakes have been proposed to have existed on Mars, including several that have been inferred to date from the Hesperian period, e.g., in Melas Chasma, Claritas Fossae, Eberswalde crater, Ismenius Cavus, and Xanthe Terra craters [e.g., Quantin et al., 2005; Mangold and Ansan, 2006; Mangold et al., 2012c; Dromart et al., 2007; Dehouck et al., 2010; Hauber et al., 2013]. The occurrence of lacustrine activity so late in early Mars history was usually considered to be limited to short-term episodes questioning the extent of the observed system at Yellowknife Bay.

Apart from the well-studied Sheepbed mudstones, the other members display various textures, dominated by sandstones [Grotzinger et al., 2014]. Much less attention has been paid to the chemistry and textures of these sandstones, except that their facies are interpreted to be of fluvial origin [Grotzinger et al., 2014]. We will not discuss further the depositional scenario of these sediments, but we propose to investigate in-depth chemical and textural variations along the entire stratigraphic section. These are fundamental observations to understand the sediment provenance(s) and diagenetic evolution of these rocks. The number of targets analyzed by ChemCam in these sediments represents a large amount of data (190 ChemCam targets corresponding to ~1400 analyzed locations and representing ~50,000 spectra) helping to build a chemostratigraphic record and a comprehensive picture of the sedimentary processes at Yellowknife Bay. The analysis of ChemCam data provides elementary chemistry on all these targets, helps to identify locally individual mineral grains and to detect the presence of hydrous minerals by analyzing the hydrogen emission peak.

After presenting the methods (section 2), a detailed context of the stratigraphy of Yellowknife Bay Formation is provided including relevant observations of individual Yellowknife Bay outcrop textures and individual ChemCam analyses (section 3). The cross comparison of each member using ChemCam analyses is the primary focus of this study and allows us to identify the main chemical differences from one outcrop to another (section 4). The discussion then focuses on the varying provenances and diagenetic evolution of each outcrop (section 5).

2. Methods

2.1. ChemCam Analyses

ChemCam is an active remote sensing instrument that uses a laser to determine the composition of rocks and soils. The technique used is referred to as Laser-Induced Breakdown Spectroscopy (LIBS), in which the energy of a laser pulse is focused on a small spot (~0.2–0.6 mm diameter) to ablate material and produce atoms in an excited state. The decay of these atoms back to ground state produces a visible plasma lasting less than 10 μ s, which is collected by three spectrometers in the UV (240–342 nm), Violet (382–469 nm), and visible/near-infrared (474–906 nm) spectral ranges. Collection of the plasma light and spectral dispersion allows identification of the characteristic emission lines of the elements present in the sample [e.g., Cremers and Radziemski, 1983, 2006].

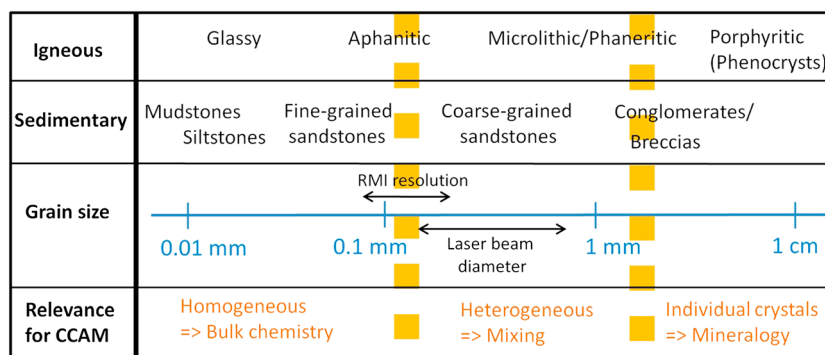


Figure 1. Sketch showing the three main size ranges of rock textures analyzed by ChemCam. Numbers are approximate and depend on distance between the laser and the targets. Below ~ 0.2 mm the grain size is smaller than the laser beam diameter, and ChemCam analyses report a homogeneous composition close to the bulk chemistry. Above 0.5 – 2 mm, ChemCam can analyze mineralogy of phenocryst grains. This can occur anytime the grains are larger than the ≤ 0.5 mm beam size, but for grain sizes close to this parameter multiple grains are still likely to be hit. For grain sizes between 0.2 and 2 mm, ChemCam analyzes a mixture of grains requiring a large statistical sampling for a determination of the bulk chemistry.

On Mars, the first laser shots remove surface dust, enabling measurement of the dust-free rock chemistry. ChemCam thus provides elemental composition information on analysis spots at distances up to 7 m from the Curiosity rover [Wiens *et al.*, 2012; Maurice *et al.*, 2012].

To date, ChemCam has identified a broad list of elements on Mars, including major elements (Si, Al, K, Na, Ca, Mg, Fe, and Ti) which are useful to determine the rock type [e.g., Sautter *et al.*, 2013a] and minor and trace elements (Li, Mn, Cr, Zn, Sr, Rb, Ba) which are useful for tracing igneous processes [Ollila *et al.*, 2013]. Volatiles and halogens (O, S, P, H, Cl, and F) are identified in rocks and soils at various levels [Meslin *et al.*, 2013; Schröder *et al.*, 2014; Forni *et al.*, 2014]. Carbon is identified at about the same level of emission for all targets analyzed so far and is interpreted as due to Mars' atmospheric contribution [Schröder *et al.*, 2014].

With a beam diameter of ~ 0.2 – 0.6 mm at the distance of analysis (usually 2 to 5 m), the ChemCam spectra do not necessarily yield a bulk rock analysis. The diameter of the laser beam implies that the interpretation of the spectra collected depends on the grain size of the rocks analyzed (Figure 1). Fine-grained sediments, such as mudstones or fine-grained sandstones, as well as glassy or aphanitic textures in igneous rocks, have grain sizes that are small enough that different observation points produce uniform spectra. In these cases the only variations are at the level of the precision of the technique [e.g., Blaney *et al.*, 2014], and a single observation, or a very small number of observations, provides the whole-rock composition (Appendices 1 and 2). In contrast, laser shots on igneous phenocrysts, or sedimentary granules derived from igneous minerals, are able to give the composition of individual grains, providing a direct mineralogical sounding. In the intermediate case, usually for grain sizes between 0.2 and 1 mm, data display a strong variability in the composition, which is related to the natural mineralogical diversity in rocks. When analyses indicate a heterogeneous sampling from location to location, data can locally be interpreted as originating from a mixture of two or three phases [e.g., Sautter *et al.*, 2013a]. In order to obtain the bulk chemistry, we limit these mixing effects by averaging the maximum number of points possible for a given outcrop or unit. Data are usually collected in lines of 5 or 10 points or matrices of 3×3 , 4×4 , or 5×5 points, spanning centimeters on the rock.

2.2. Classification and Quantification

Quantification of major elements in oxide weight percent can be done through two different approaches, known as multivariate analysis or univariate analysis [e.g., Wiens *et al.*, 2013]. The former method is generally used with major elements and the latter for minor and trace elements [Ollila *et al.*, 2013; Cousin *et al.*, 2014]. Most elements have at least several emission peaks within the spectral range (240 – 905 nm) covered by ChemCam. Multivariate analyses take advantage of this large spectral range by considering that the observed spectra are linear combinations of pure element sources and that the simultaneous analysis of several emission peaks gives a better statistical sampling of the proportion of a given element than does the analysis of individual peaks. A commonly used method is the Partial Least Squares regression (PLS) in which spectra are compared to known standards analyzed in a test bed on Earth [Clegg *et al.*, 2009]. A detailed description of this method is provided in Appendix B.

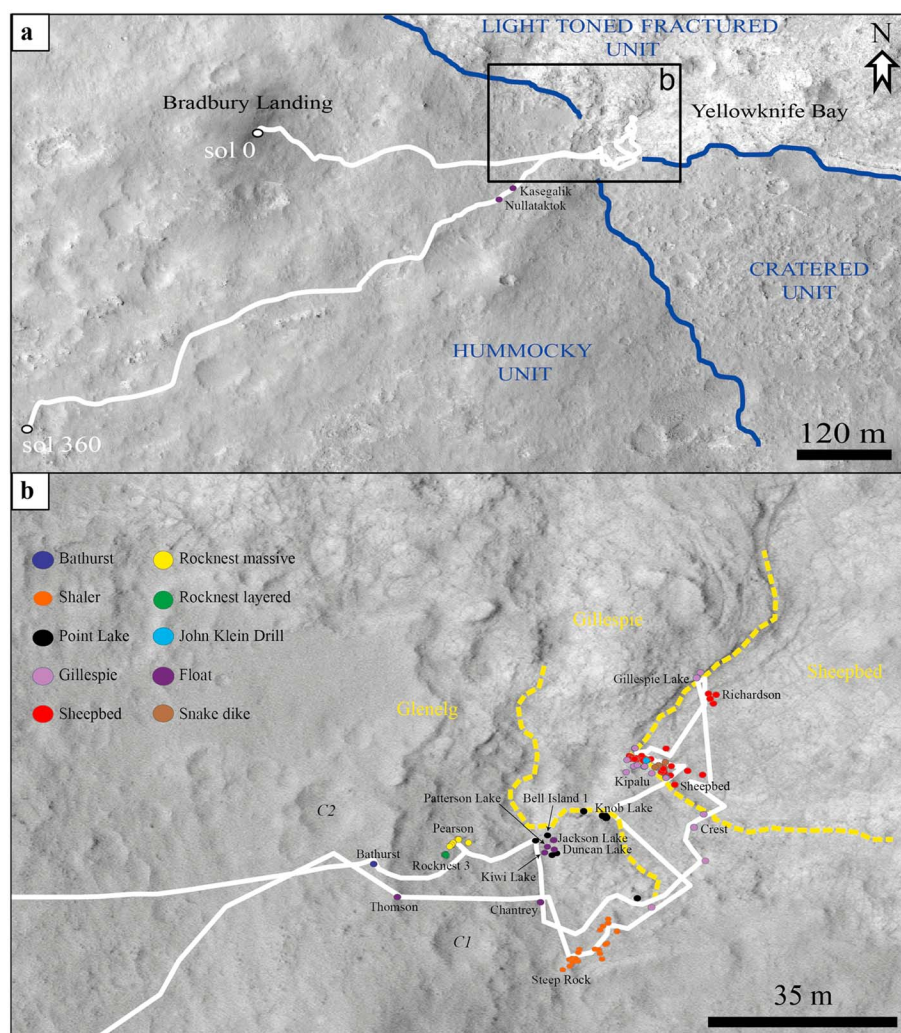


Figure 2. (a) Close-up of a HiRISE image of the Bradbury landing site and the Glenelg area (HiRISE image PSP_010573_1755). (b) Local simplified map of Yellowknife Bay sediments with ChemCam targets superimposed. Each color group corresponds to defined members or facies as reported in Table 1, Appendix A, and in the text.

Independent component analysis (ICA) is a statistical and computational technique for revealing hidden factors that underlie sets of random variables, measurements, or signals [Comon, 1994; Hyvärinen *et al.*, 2001] (see Appendix B for details). Because ICA is a powerful method for cross comparisons, it will be used for inspecting the whole set of points simultaneously, especially for qualitatively assessing the variability of the composition of each group of outcrops. The ICA method is also helpful for detecting hydrogen using the 656 nm emission line. Quantitative hydrogen estimation is a complex problem in LIBS analysis due to its apparent strong dependence on matrix effects (i.e., variations in optical and mechanical properties from one rock to another) [Sobron *et al.*, 2012; Schröder *et al.*, 2014]. However, it is expected that multivariate approaches such as ICA partly compensate for these effects. Comparison of relative hydrogen abundances can be estimated using the proposed semiquantitative estimation with ICA plots.

2.3. Imaging Data Sets

The ChemCam instrument suite includes a Remote Microimager (RMI) which provides context imaging with submillimeter spatial resolution [Wiens *et al.*, 2012; Maurice *et al.*, 2012; Le Mouélic *et al.*, 2014]. Images are routinely taken before and after the LIBS analyses, providing a view of the points analyzed and of the morphology and texture of the material hit. The RMI has an angular pixel size of 0.0196 mrad/pixel and a circular field of view of 20 mrad (1.15°) over 1024 × 1024 pixels providing a spatial sampling of ~0.04 mm/pixel to

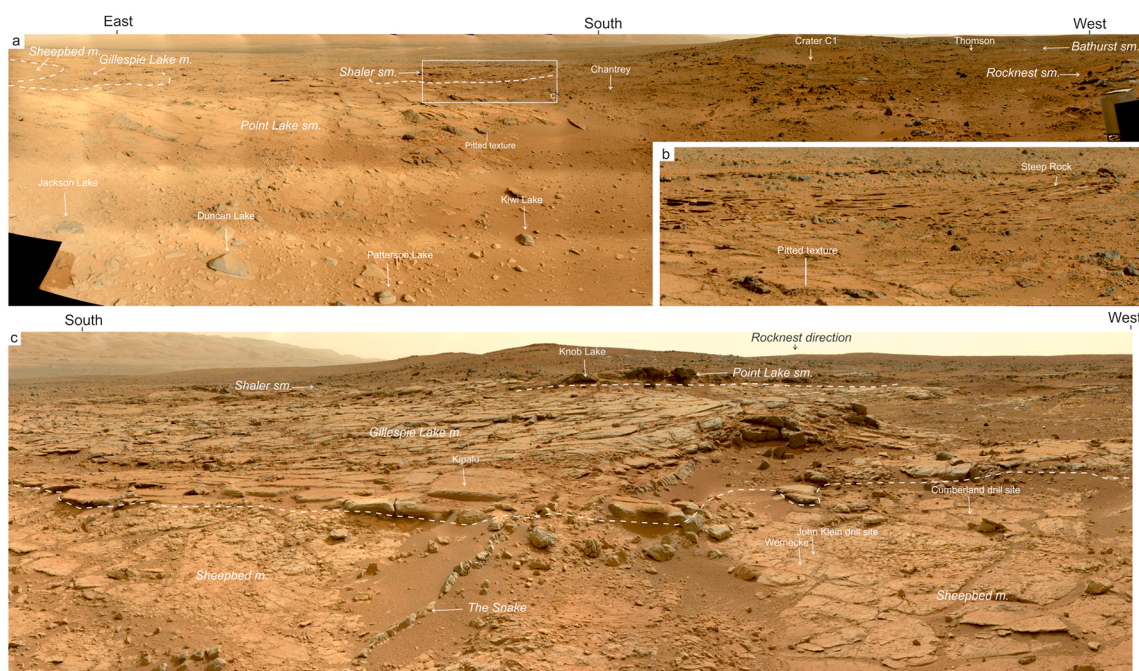


Figure 3. (a) Mosaic of the Glenelg member taken on sol 106 shortly after leaving the Rocknest area (Mastcam images 0106ML0006810xx0103yyyE01 with xx ranging from 09 to 80 and yyy ranging from 043 to 114). Targets noted in the images are layered float rocks and individual targets presented in the paper. m. = member, sm. = submember. (b) Close-up of the Shaler outcrop showing laminated layers over a vertical rise of 1–1.5 m. (c) Mosaic of the Sheepbed and Gillespie members taken on sol 137 before stopping to drill at John Klein (Mastcam images 0137ML0008180xx0104yyyE01 with xx ranging from 06 to 45 and yyy ranging from 151 to 190). The dashed line separates the smooth recessive layers of the Sheepbed member from the protruding Gillespie Lake sandstone and from the darker pitted texture of the Point Lake outcrop. Shaler and Rocknest directions are indicated but the outcrops are not visible due to the lower topographic position of the scene.

~0.15 mm/pixel in the distance considered for LIBS analyses (2–7 m) [Le Mouélic *et al.*, 2014]. Other sets of images were used to analyze textures to provide a better context for the ChemCam observations and, more generally, to characterize the rocks studied. The MastCam instrument is composed of two cameras. The left Mastcam (M-34) has a 34 mm focal length, a 0.22 mrad/pixel image scale, and an $18.4^\circ \times 15^\circ$ effective field of view (FOV) over 1600×1200 pixels. The right Mastcam (M-100) uses a similar charge-coupled device (CCD) and has a 100 mm focal length, a 0.074 mrad/pixel image scale, and an effective FOV of $6.3^\circ \times 5.1^\circ$ over 1600×1200 pixels [Malin *et al.*, 2010; Bell *et al.*, 2012]. The Mars Hand Lens Imager (MAHLI) is a 2 megapixel color CCD camera with a macrolens that can focus over a range of distances from 2.1 cm to infinity [Edgett *et al.*, 2013]. MAHLI was designed for investigating geologic materials at the hand lens scale. A standard image of 1600 by 1200 pixels provides a field of view of about 2.3 by 1.7 cm at closest focus, with a spatial resolution of 14 μm /pixel [Edgett *et al.*, 2013].

3. Stratigraphy, Facies, and Individual Analyses

3.1. Geological Setting and Stratigraphic Section

The rover encountered the three members (Sheepbed, Gillespie Lake, and Glenelg) in reverse-stratigraphic order (Figure 2). A stratigraphic column representing the stratigraphy of the Yellowknife Bay formation was presented by Grotzinger *et al.* [2014] in one single column. In this section we propose that two columns, with a northern and a southern section, give a more accurate representation of the lateral and vertical facies observed.

The Glenelg member displays four main outcrops: Point Lake, Shaler, Rocknest, and Bathurst Inlet. These outcrops exhibit different lithological characteristics and are difficult to trace laterally over distances greater than a few tens of meters, in HiRISE and Curiosity images. Figure 3a shows a panorama (collected on sol 106) facing south and taken after the Bathurst Inlet and Rocknest outcrop analyses. Rocknest is located to the west, with Bathurst Inlet being even further west. In the left and central foreground, several float rocks analyzed by ChemCam are seen. Just behind these rocks, an outcrop with a pitted texture represents the

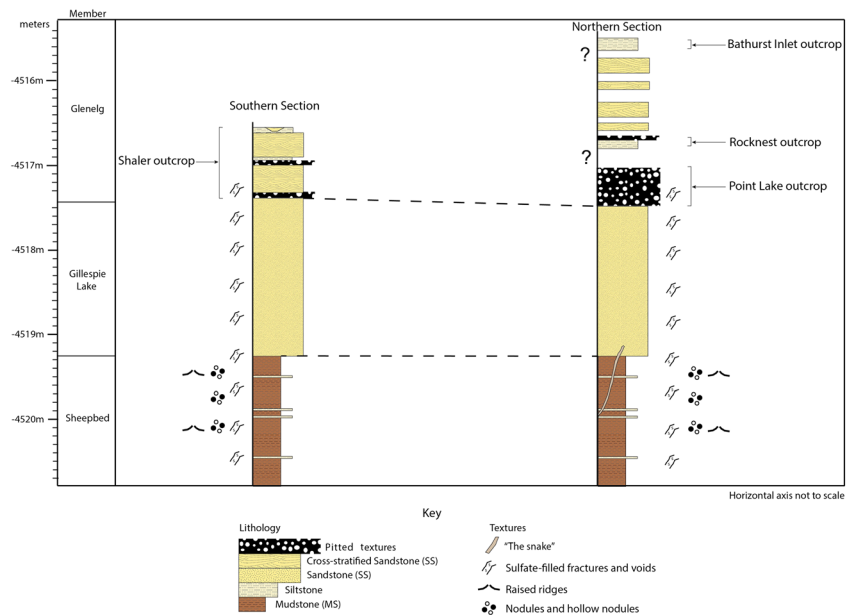


Figure 4. Two-column representation of the Yellowknife Bay stratigraphy (adapted from Grotzinger *et al.* [2014]). Although the horizontal axis is not to scale, these sections are separated by ~30 m at their base. The occurrence of several key diagenetic textures throughout the sections measured at Yellowknife Bay is also annotated, although they are not discussed in-depth in this study. See text for explanations.

typical facies of the Point Lake outcrop. Several tens of meters away lies the Shaler outcrop, which displays platy layers, as shown in the close-up in Figure 3b. Shaler sits above the pitted texture from Point Lake, but this facies cannot be followed laterally. The left (east) side of the mosaic in Figure 3a shows the topographically lowest areas containing the Gillespie Lake and Sheepbed members. Figure 3c shows a mosaic of images taken on sol 136. The Sheepbed-Gillespie Lake member contact was defined by the transition from the recessive layer to the more resistant, overhanging layers which were also visible from orbital data. Gillespie Lake is overlain by the Point Lake outcrop, observable in the background at the top center of the panorama, though this contact is not always visible (Figure 3c). In the far background of Figure 3c, the change in roughness corresponding to the regolith-covered hummocky plains is observed.

Given several north-south changes in exposure, a two-column section represents more precisely the observed stratigraphy (Figure 4). The northern section includes, from bottom to top, the Sheepbed and Gillespie Lake members, and the Glenelg member composed of Point Lake, Rocknest, and Bathurst Inlet outcrops (Figure 4). Outcrop exposure is continuous throughout the lower half of the section, from the Sheepbed member through the Point Lake outcrop, but outcrops are discontinuously exposed between the Point Lake and Bathurst Inlet outcrops, such that their continuity is uncertain. The southern section includes the Sheepbed and Gillespie Lake members, overlain by a thinner outcrop in lateral continuity with the Point Lake outcrop and by the Shaler outcrop. Shaler contains a heterogeneous assemblage of facies including interstratified coarser-grained sandstones and pebble beds, recessive finer-grained intervals, and several layers with a pitted texture similar to that of the Point Lake outcrop (Figure 4). We will refer to these pitted textures in the following section.

3.2. Individual Member Analysis

In this section, we describe the characteristics of each member of the Yellowknife Bay formation in stratigraphically ascending order. Targets have been chosen to provide examples of spectra and images of key outcrops useful for the discussion of the chemical variations. Detailed chemical analyses of two of these outcrops (Rocknest and Shaler) are provided in other papers focusing exclusively on these outcrops [Blaney *et al.*, 2014; Anderson *et al.*, 2014].

The Sheepbed member was the only member in which drilling (two sites) and brushing (three sites) were performed (Figures 5 and 6). A number of diagenetic features were found in Sheepbed, including nodules [Stack *et al.*, 2014], calcium sulfate veins [Nachon *et al.*, 2014], mm size Mg-rich raised ridges [Léveillé *et al.*, 2014],

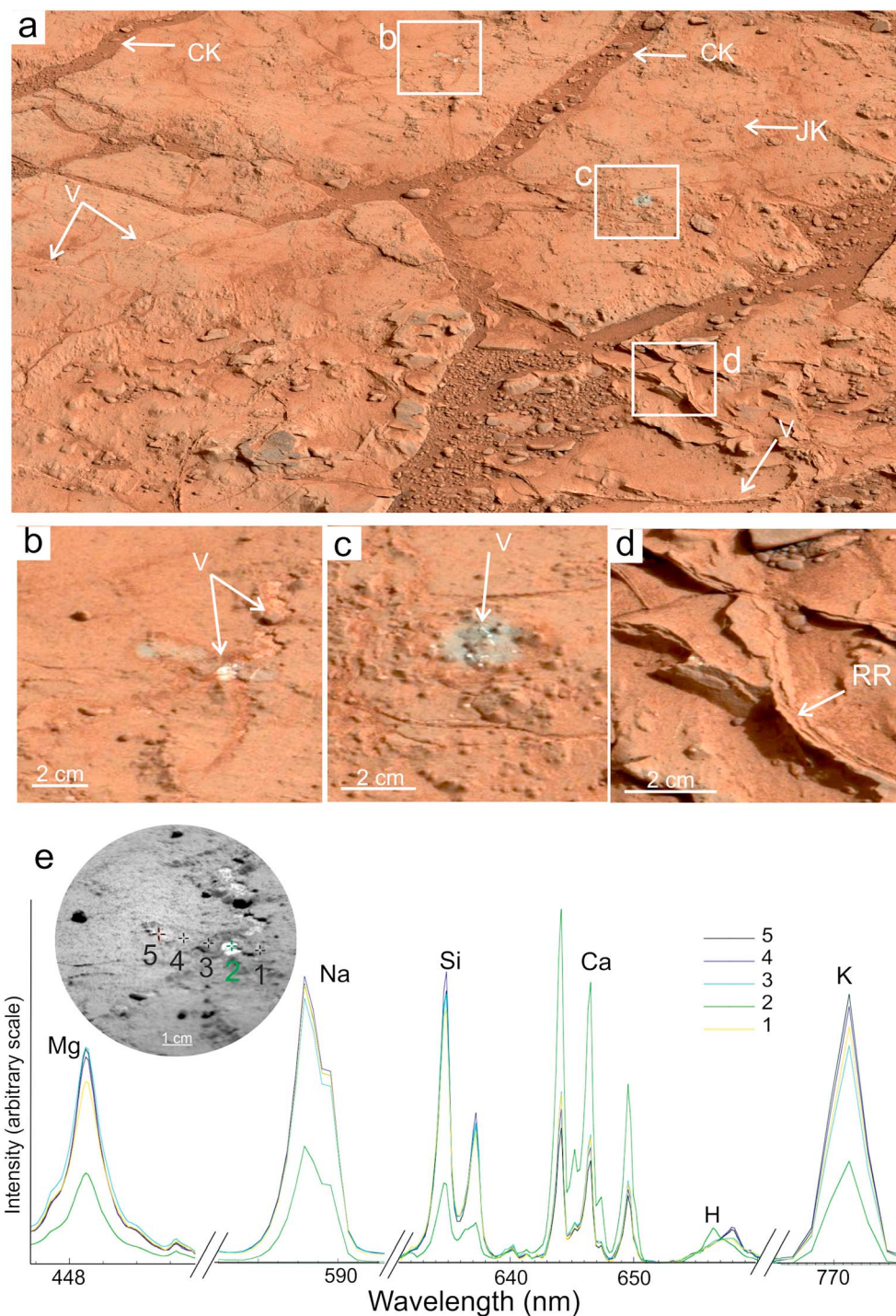


Figure 5. (a) Mosaic of the Sheepbed mudstone at the John Klein drill area (taken before drilling on location JK, Mastcam images 0166MR0008880xx0201yyyE01 with xx ranging from 00 to 14 and yyy ranging from 629 to 643). CK: Open cracks filled by sand. V: Veins that are filled by calcium sulfates. (b) Close-up of ChemCam targets DT-RP6 taken after the ChemCam analysis was done (raster of five locations) showing the area that was blasted by the laser shot in gray. (c) Close-up of ChemCam targets DT-RP5 after four locations with depth profiles (150 shots). Both close-ups show the light-toned sulfate-rich material better when free of dust. (d) Close-up of the Mc Grath target before analysis by ChemCam. The curved shape with thin multiple layers is typical of raised ridges (RR). (e) Selected emission lines of the ChemCam spectra of the DT-RP6 target with the RMI image as an inset (image number CR0_412228167EDR_F0052270CCAM02166M). The second point where the material is brighter shows enrichment in calcium interpreted as calcium sulfates [Nachon *et al.*, 2014]. Other points are homogeneous in composition. Hydrogen is absent except for the calcium-rich spectra. Intensity is relative to each portion of the spectra.

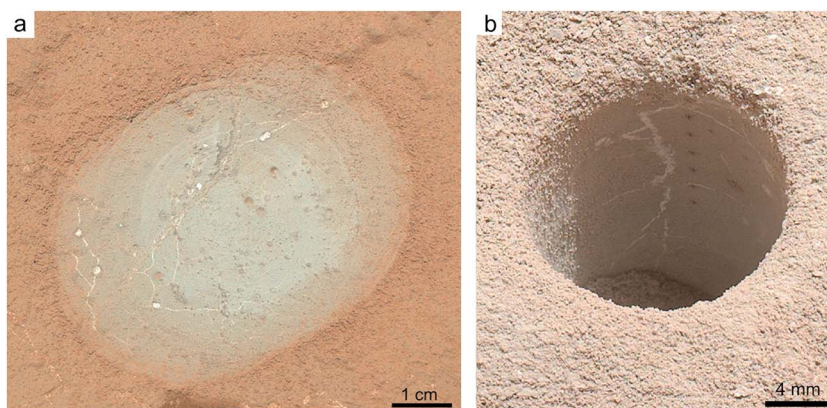


Figure 6. (a) Wernecke brushed area (portion of MAHLI image 0169MH0002050010102201C00) (b) Close-up of the 1.6 cm wide drill hole (Focus merged image of 7 MAHLI images 0270MH000254005010279nC00 with n from 2 to 9) showing darker LIBS spots down far wall of hole next to light-toned calcium sulfate veins.

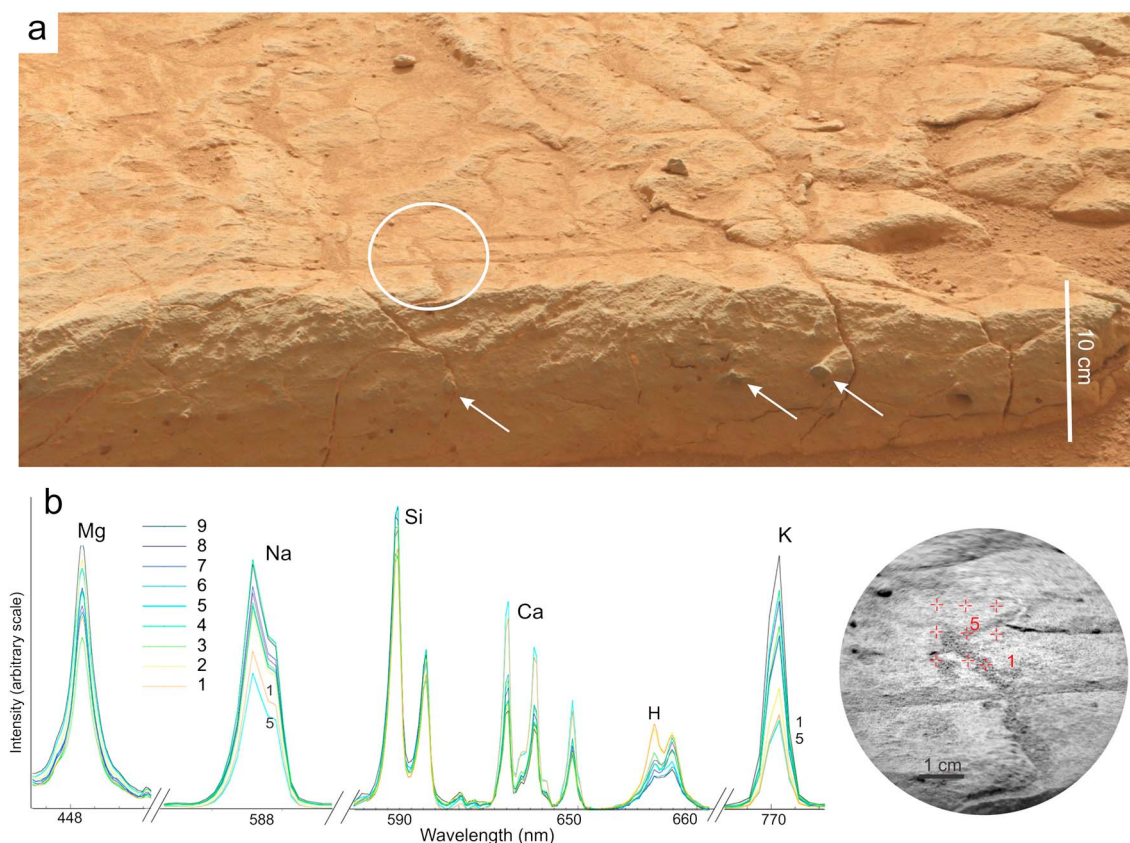


Figure 7. (a) Mosaic of the ChemCam target Kipalu, part of the Gillespie sandstone, taken on sol 153 (MastCam images 0153MR0008500000201268E01 and 0153MR0008500010201269E01). The 10 cm high rock front contains centimeter-size pebbles. A series of cracks cross the rock; these are less in extent at Gillespie than Sheepbed. Over the nine locations analyzed by ChemCam at the top of the Kipalu target, locations 1 and 5 sampled local soils (RMI image CR0_411429665EDR_F0051954CCAM03157M). Distinct spectra are observed for these two points in the soil, showed by enhanced Ca and Mg, and depleted Na (b). These points are likely mafic grains in the soil. These two points were not taken into account for determining rock chemistry (Appendix B). Spectra of the rock appear rather homogeneous, perhaps with more variability in K. Hydrogen is present in the soil, and to a lesser amount in all the points targeted. The intensity is relative to each portion of the spectra.

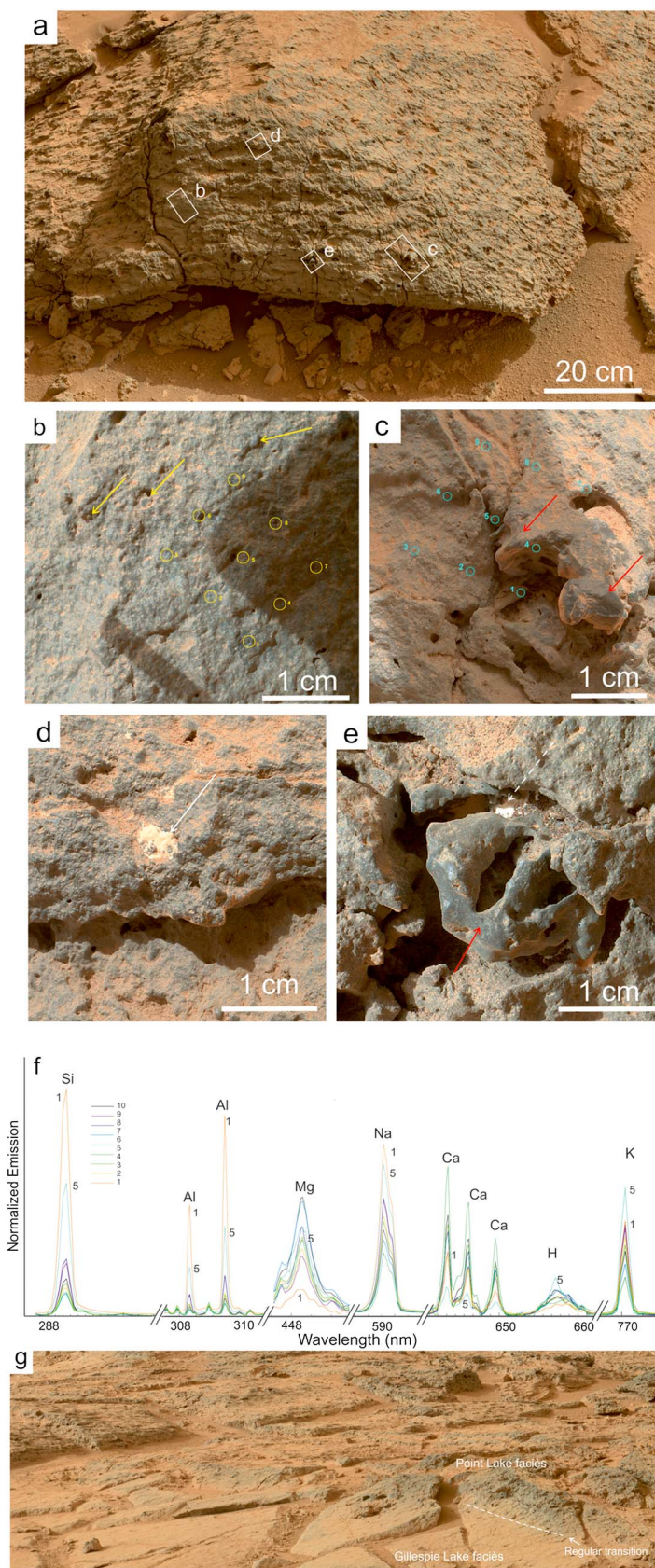


Figure 8

and a 10 cm wide sedimentary dike, named The Snake, and supposed to be formed by injection of fine-grained sediments from underlying layers [Grotzinger *et al.*, 2014]. The highest-resolution (20–30 $\mu\text{m}/\text{pixel}$) MAHLI images (e.g., Wernecke and drill hole images, Figure 6) show a lack of well-defined grains. This observation demonstrates that the Sheepbed member is characterized by fine grains (clay size or silt size), suggesting it is a mudstone. The spectral plot in Figure 5e shows depletion in all major elements (Mg, Na, Si, and K) except Ca, and a slight hydrogen peak, typical of hydrated calcium sulfates. The four other points have identical compositions (Appendix B) likely due to the relatively homogeneous chemistry of the bulk rock.

The Gillespie Lake member, located above the Sheepbed member, consists of poorly defined beds formed of poorly sorted, subangular, fine- to medium-sand sized grains (100–500 μm) [Grotzinger *et al.*, 2014]. This member is nevertheless not homogeneous in texture. Figure 7 shows that the outcrop Kipalu (see Figures 1 and 2c for context) has 1–3 cm diameter gravels/pebbles embedded within a much finer-grained rock. The outcrop displays a dozen of these >1 cm gravels/pebbles on the 0.1 m^2 area of the Kipalu face, which remains a statistically low number. These pebbles are somewhat smooth, likely because of mechanical rounding. Accordingly, Kipalu can be classified as a pebbly sandstone. ChemCam laser shots did not sample large individual gravels either at Kipalu or at the >100 other locations sampled at Gillespie Lake, likely because gravels/pebbles are scarce and no specific targeting was done to analyze their composition. The spectra from Kipalu all look similar (Figure 7), with only limited variations in the major elements (see also Appendix B), suggesting the grain size is small enough to avoid significant compositional variations.

The Glenelg member includes several outcrops of various facies that are above the Gillespie Lake member. These are from bottom to top, Point Lake, Shaler, Rocknest, and Bathurst. The Point Lake outcrop has not been described in detail in earlier studies. It is a resistant dark-toned rock (~ 0.5 m thick) located immediately above the Gillespie Lake member (Figure 8). It displays pitted textures with voids from millimeters to several centimeters in average diameter and typically lacks obvious sedimentary grains (Figures 8a–8e). A careful examination of MAHLI images nevertheless enables the identification of few grains of 0.5–2 mm in size (yellow arrows in Figure 8b). The presence of these coarse grains shows that the outcrop is a strongly cemented sediment, such as a coarse or very coarse sandstone. ChemCam spectra at Point Lake display a large variability, especially when compared to lower members (Figure 8f). The example of Knob Lake reveals two points (1 and 5) for which the major elements Si, Al, Na, and K are enhanced compared to the overall rock (Figure 8f).

The Shaler outcrop (1 to 1.5 m thick) lies stratigraphically above the uppermost Point Lake facies (Figures 3b and 9). It consists of a heterogeneous assemblage of interbedded platy coarse-grained sandstones separated by recessive intervals. The cross-bedded texture of the Shaler outcrop was not encountered in such detail elsewhere. Parts of the Shaler outcrop also show a distinct pitted texture (Figure 9c) somewhat similar to that observed at Point Lake. The chemistry of the Shaler outcrop is strongly heterogeneous compared to other members, likely due to the large variability in the grain size encountered. For the example of Steep Rock selected in Figure 9g, the Mg emission lines display strong variability not observed at the Gillespie Lake or Sheepbed members. Location 11 in particular displays a distinct composition with enhanced Si, Al, Na, and K emission lines compared to other points of Steep Rock. This point has the same characteristics as the points 1 and 5 from Knob Lake.

A common feature of the Point Lake and Shaler outcrops is the presence of pitted textures. At Point Lake, MAHLI images show that the rock is relatively rough with pits and protrusions being observed at different locations (Figure 8b). A frequent observation is that the Gillespie Lake sandstones transition gradually

Figure 8. (a) Mosaic of part of the Point Lake outcrop (sol 303) (Mastcam images 0303MR0012610xx0203yyyE01 with xx ranging from 00 to 44 and yyy ranging from 818 to 862). (b–e) Close-ups from MAHLI images of the Point Lake outcrop. MAHLI images 0304MH0002950000103928R00 in Figure 8b, 0303MH0002890000103778R00 and 0303MH0002890000103780R00 in Figure 8c, 0303MH0002900000103786R00 in Figure 8d, and 0304MH0002650000103910R00 in Figure 8e. In Figures 8b and 8c circles indicate where ChemCam shots were aimed, respectively, on targets Balboa and Knob Lake. Although texture is massive in Figure 8b, local grains 0.5–2 mm wide are present (yellow arrows). Points 1 and 5 in Figure 8c are those enhanced in alkali feldspar compositions as detected in the spectra in Figure 8f. The protruding shapes (red arrow) in Figures 8c and 8e display a distinct smooth, homogeneous texture. This close-up shows a 5 mm wide light-toned spot (arrow) corresponding to a calcium sulfate nodule (as determined by ChemCam; Figure 8d) [Nachon *et al.*, 8]. A similar light-toned spot is observed in Figure 8e (dashed white line). (f) Selected emission lines of the spectra corresponding to locations shown in Figure 8c. Intensity is relative to each portion of the spectra. (f) Mosaic (sol 306) showing the regular transition between the homogeneous smooth texture of the Gillespie member and the Point Lake member (MastCam images 0306MR0012670xx0203yyyE01 with xx ranging from 00 to 17 and yyy ranging from 930 to 947).

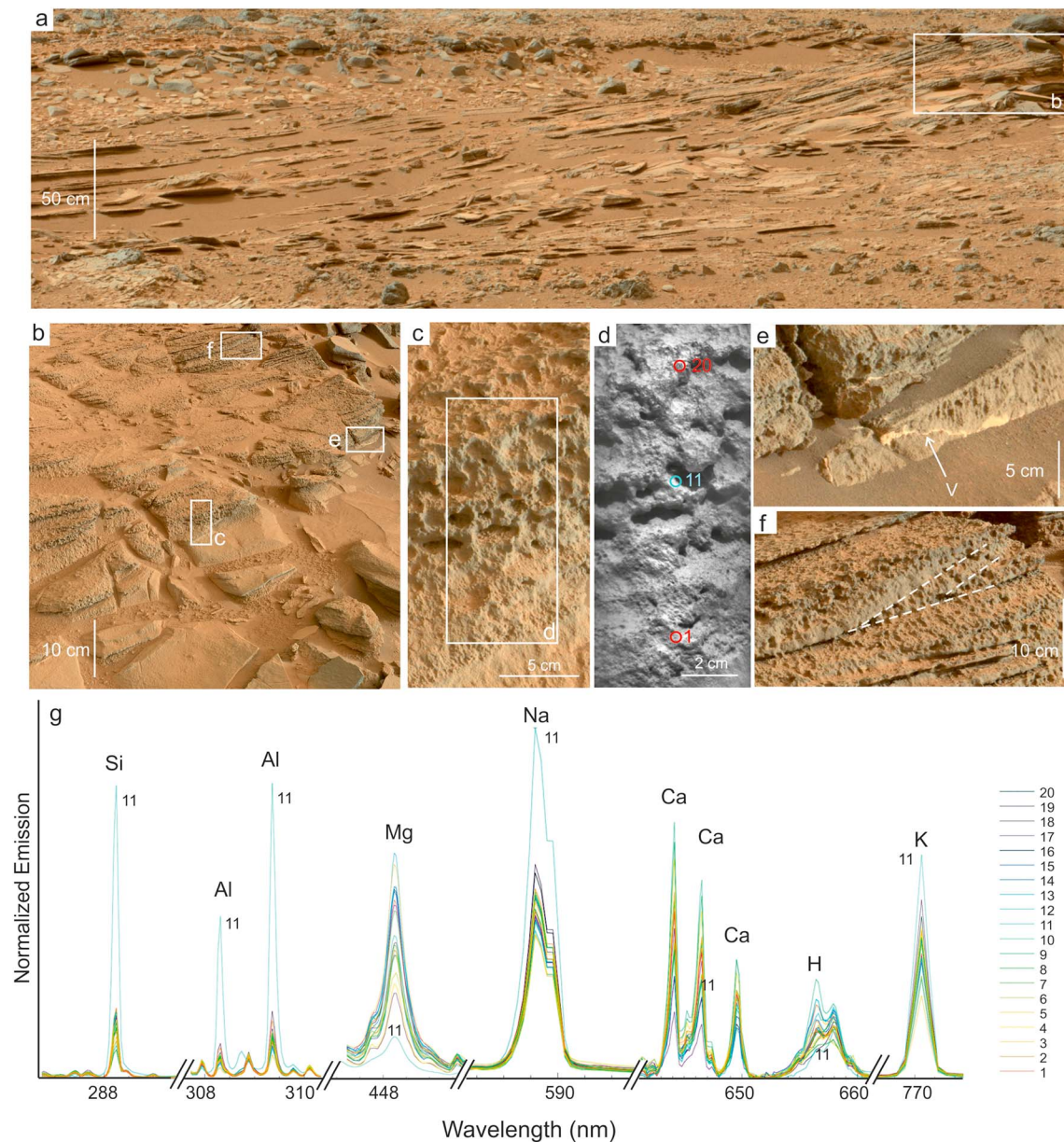


Figure 9. (a) Mosaic of Shaler outcrop taken on sol 110 (MastCam images 0110MR0006860xx0200yyyE01 with xx from 30 to 34 and yyy ranging from 333 to 337). (b) Mosaic of part of the Shaler outcrop taken on sol 318 (Mastcam images 0318MR0013040xx0300yyyE01 with xx from 00 to 97 and yyy ranging from 706 to 803) viewing the outcrop from above compared to the far view in Figure 9a. (c and d) The center and top right of the mosaic show a pitted texture that is shown at a higher resolution using ChemCam/RMI images CR0_426170755EDR_F0060804CCAM02323M, CR0_426169619EDR_F0060804CCAM02323M, and CR0_426168545EDR_F0060804CCAM02323M. This texture, corresponding to the target Steep Rock, shows a continuous trend with surrounding layers. (e) Calcium sulfate vein fills cracks in Shaler but to a lesser extent than in other areas. (f) Close-up showing the pitted texture with cross bedding. (g) ChemCam spectra of selected emission lines of the target Steep Rock presenting a large internal variability. Location 11 reveals enhanced Si, Al, Na, and K, suggesting local enrichment by alkali feldspar. Hydrogen is present at all points except for the alkali-rich point. Intensity is relative to each portion of the spectra.

(dotted lines in Figure 8g) into the more pitted Point Lake facies. At Shaler, some outcrops were locally similar to the Point Lake outcrops (compare Figures 9f and 8g). The pitted texture is most prevalent in the coarsest-grained sandstones and varies laterally across the outcrop. Outcrop sections without pitted texture include thin resistant beds separated by recessive intervals.

The Rocknest area is composed of several outcrops separated by a modern eolian bedform, the loose material of which was analyzed by CheMin and Sample Analysis at Mars [Blake *et al.*, 2013]. A detailed investigation of chemistry of this outcrop has been done by Blaney *et al.* [2014] and only a short summary of its facies and

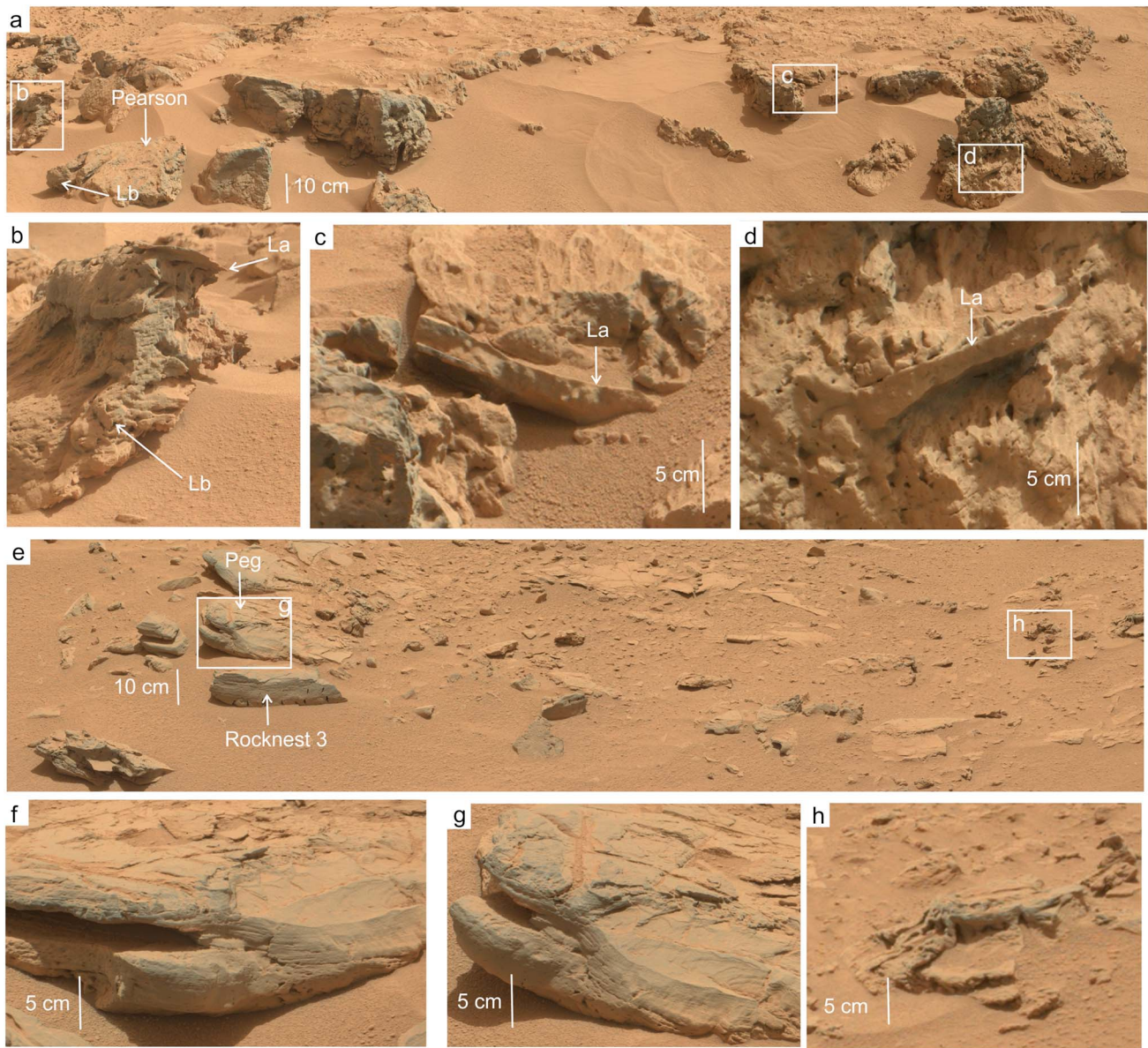


Figure 10. (a) Mosaic of the Rocknest outcrop showing massive boulders with widespread voids or vugs as well as lobate shapes (Lb) (Mastcam images 0078MR0005760xx0103835E01 with xx ranging from 00 to 60 and yyy ranging from 835 to 895). (c and d) Small layers (La) are embedded inside the mass of the rock. (e) Mosaic of the Rocknest area on the other side of the Rocknest sand shadow (Mastcam images 0059ML0002690xx0102yyyE01 with xx from 00 to 10 and yyy ranging from 305 to 308). Here the 10–15 cm high rocks are layered with thin several millimeters thick parallel laminations. (f and g) The rock Peg taken from two different perspectives at a nearly 90° difference in view angle (f) MastCam image 0056MR0002580000103086E01. Cracks at the top do not propagate far inside the rock. (h) Image showing a deformed layer, which is located 2 m left of the rock Pearson visible in Figure 10a. It marks a transition from the layered area to the massive and lobate part of Rocknest.

setting is given here to highlight differences with the other outcrops. The Rocknest outcrops display two distinct textures. A massive 40–50 cm thick outcrop surrounded by in-place boulders is exposed on the northern side of the Rocknest area. In contrast to this massive outcrop, a series of 15 cm thick finely laminated rocks are exposed a few meters to the southwest (rocks named Peg and Rocknest 3 in Figures 10e–10g). The few millimeters thick laminations run parallel to the soil surface, suggesting that the rocks are in place. Several centimeter thick pieces of bedded material (apparently displaced layers) are embedded inside the northern outcrop (Figures 10c and 10d).

The Bathurst Inlet outcrop (hereafter referred to simply as Bathurst) corresponds to a group of rocks that were fractured and modified by weathering. Bathurst was analyzed by *Schmidt et al.* [2014] in comparison with

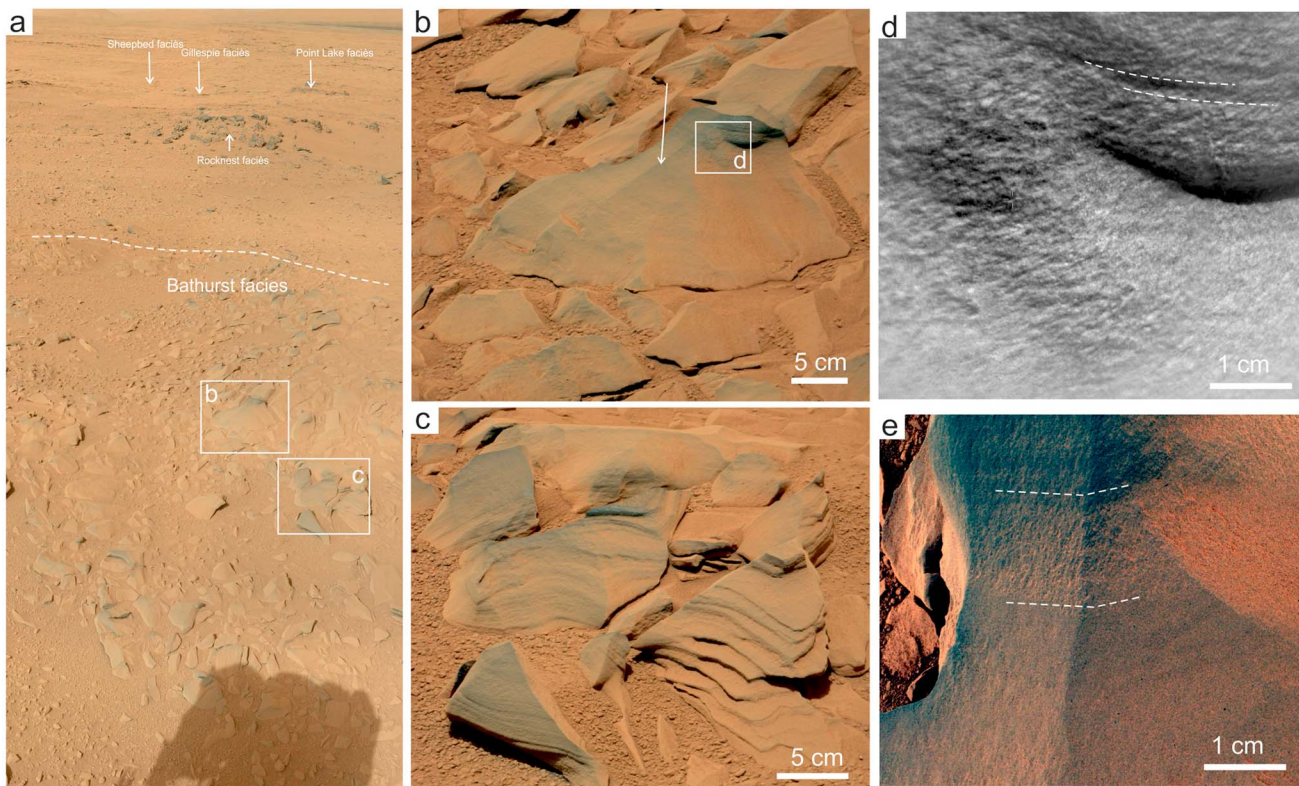


Figure 11. (a) MastCam mosaic of Bathurst area showing Rocknest in second plan and the Yellowknife Bay area toward the bottom of the topography. Images 0052ML0002400xx0102yyyE01 with xx ranging from 0 to 9 and yy ranging from 210 to 219. (b) Bathurst is a 10 cm high rock with a sharp edge and dust mantling limiting a view of its texture. MastCam image 0053MR0002430000102993E01. (c) MastCam image 0053MR0002450000102994E01 of the rocks near Bathurst showing millimeter thick laminations. (d) ChemCam/RMI close-up showing smooth texture with barely visible laminations (dashed lines). (e) MAHLI image (0054MH0000190000100356R00) taken from above the Bathurst crest showing the polished surface and these millimeter thick laminations (dashed lines).

igneous float rocks, but not in the framework of Yellowknife Bay formation. Bathurst is the uppermost stratigraphic layer at the top of the Glenelg member (Figure 11), although the location of its lower contact relative to the underlying parts of Glenelg is uncertain. Ten centimeter high rocks such as those of the Bathurst target display a dusty appearance with sharp edges suggesting resistant rocks that fracture along planar surfaces that are then sculpted by wind (Figure 11b). Lamination at Bathurst outcrop is very subtle, even at RMI or MAHLI scales (Figures 11d and 11e), but it is obvious in surrounding rocks where differential erosion is more pronounced (Figure 11c). The layering revealed there shows several millimeters thick parallel laminations of fine-grained material. Only one raster of five points was performed by ChemCam with negligible variations among the five points analyzed (Appendix B).

3.3. Layered Float Rocks Along the Traverse

Float rocks were regularly targeted by ChemCam along the rover traverse. They are diverse rocks with varying properties, from coarse grained to fine grained. Some massive float rocks were interpreted to have igneous origins based on texture and composition [Sautter *et al.*, 2013a; Yingst *et al.*, 2013]. Because this study is focused on the in-place sandstone deposits at Yellowknife Bay, the eight float rocks discussed below were selected based on their bedded/laminated texture similar to in-place outcrops within the Glenelg area. These rocks were encountered along the margin of Yellowknife Bay, on sols 110–117, at the transition from the Rocknest area to the Point Lake outcrop, and on sols 326–336, at the transition from Shaler to the hummocky plains (Figures 2 and 12). It will be shown in the next section why these float rocks are important.

Layering is obvious in Kiwi Lake, Kasegalik, Chantrey, Nullaktatok, and Thompson (respectively Figures 12e and 12f, 12k and 12l, 12m and 12n, and 12g and 12h) generally consisting of several millimeter thick layers that are usually parallel, morphologically similar to the erosionally enhanced layers seen at Bathurst. Float rocks analyzed by ChemCam display easily visible laser ablation pits. These ablation pits are 0.4–0.8 mm in

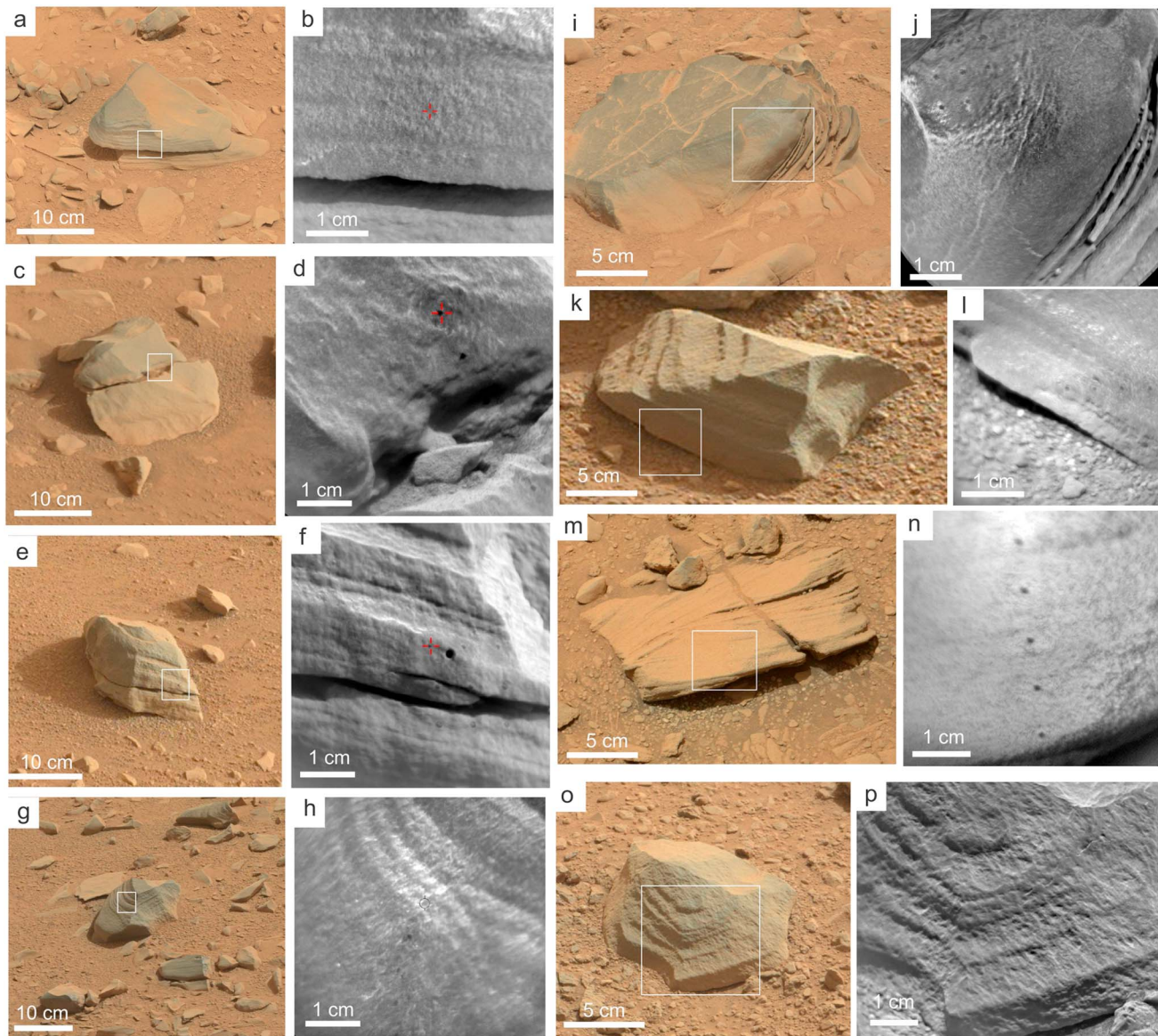


Figure 12. MastCam and ChemCam/RMI images of the layered floats observed along the rover traverse. (a and b) Duncan Lake, mosaic of Mastcam images 0112MR0006920020200529E01, 0112MR0006920030200530E01, 0112MR0006920160200543E01, and 0112MR0006920170200544E01. (c and d) Patterson Lake. Mastcam image 0106ML0006810770103111E01. (e and f) Kiwi Lake. MastCam image 0118ML0007320240103753E01. (g and h) Thompson. MastCam image 0327ML0013290150107895E01 (i and j) Jackson Lake. MastCam image 0114MR0006990070200606E01. (k and l) Kasegalik. MastCam image 0335MR0013510000301054E01. (m and n) Nullaktatok. Image 0336MR0013560000301059E01. (o and p) Chantrey. MastCam image 0326MR0013230000301002E01.

diameter, in the upper end of the range of pit sizes observed on rocks, indicating a relatively soft material [see *Arvidson et al.*, 2014]. Nullaktatok is the only float rock among the eight examined here that presents cross bedding (Figures 12m and 12n). Layering in some targets is rather faint, as observed at Chantrey and Duncan Lake (Figures 12o and 12p and 12a and 12). This faint layering is similar to the layering observed at Bathurst. Patterson Lake (Figures 12c and 12d) was selected based on its similarity to the other rocks such as Duncan Lake, and a faint layering is present from the top left to the bottom right of the block on the MastCam image, although it is certainly the least obviously layered of the float rocks selected for this study. Jackson Lake (Figures 12i and 12j) displays a curved shape at its right edge that may be considered curvilinear lamination. Nevertheless, the sharp edge suggests that fracturing may have occurred due to repeated temperature variations. Lastly, several float rocks are located in the vicinity of Bathurst (Figures 1 and 2). We interpret some of those float rocks to be ejecta associated with small craters (such as C1 and C2 in Figure 2). The mosaic in Figure 3a displays these blocks lying over a portion of the Point Lake facies, confirming this interpretation.

Table 1. ChemCam Average Bulk Chemistry in Weight Percent of Oxides^a

Member	Outcrop	Number of Points Analyzed	SiO ₂	TiO ₂	Al ₂ O ₃	FeO _T	MgO	CaO	Na ₂ O	K ₂ O	Total
Sheepbed	Full member	480	46.2	1.1	8.1	16.9	6.1	6.3	2.4	0.6	87.6
Sheepbed	The Snake (dike)	23	45.8	0.9	7.3	18.1	4.9	5.3	2.3	0.2 ^b	84.7
Gillespie lake	Full member	97	45.4	1.1	7.6	17.6	6.2	6.0	2.2	0.3 ^b	87.1
Glenelg	Point Lake	105	47.0	1.0	8.6	17.7	3.5	6.4	2.6	0.9	87.5
Glenelg	Shaler	190	45.6	1.0	7.6	18.0	5.1	6.7	2.2	0.7	87.7
Glenelg	Rocknest	130	50.9	1.2	7.3	20.5	1.4 ^b	4.9	1.9	0.9	89.0
Glenelg	Bathurst	5	46.6	1.5	7.4	18.0	7.6	5.8	1.9	1.1	90.0
Layered floats		116	47.4	1.3	8.1	18.2	6.8	6.0	2.3	1.1	91.2
<i>Glenelg</i>	<i>Shaler layered</i>	<i>130</i>	<i>45.5</i>	<i>1.0</i>	<i>7.4</i>	<i>17.9</i>	<i>5.5</i>	<i>6.6</i>	<i>2.2</i>	<i>0.7</i>	<i>86.8</i>
<i>Glenelg</i>	<i>Shaler pitted</i>	<i>60</i>	<i>45.9</i>	<i>1.1</i>	<i>7.9</i>	<i>18.1</i>	<i>4.3</i>	<i>6.9</i>	<i>2.1</i>	<i>0.7</i>	<i>86.9</i>

^aThe two last rows split the Shaler outcrop in two distinct facies, the layered Shaler (usually nonpitted) and the pitted texture at Shaler (as shown in Figure 7 at Steep Rock). All spectra acquired on diagenetic features (e.g., veins, nodules, raised ridges) were removed in order to establish the composition of the host rock themselves, with the exception of the Snake dike that is classified separately. A large number of locations were also removed (Appendix A) based on RMI images indicating that the laser hit soil or loose pebbles rather than in-place rock (e.g., points 1 and 5 on Kipalu, Figure 7). Totals are typically 85–90 wt %, for the major elements, probably due to the presence of elements not taken into account by the model such as sulfur, phosphorus, chlorine, fluorine, manganese, and hydrogen (see Appendix A).

^bThese values, much below the RMSEP (Table 2) for these elements, may not reflect accurate composition.

4. Chemical Variations of the Yellowknife Bay Formation

To provide complementary viewpoints, we use two data reduction methods:

1. The multivariate PLS analysis is used for assessing bulk chemistry of the main members/submembers of the sedimentary deposits and for enabling a relative comparison of the major element chemistry compared to a reference taken in the Sheepbed mudstones (which contains the largest statistical sampling of ChemCam data).
2. ICA plots are used for cross comparisons of all ChemCam points obtained on Yellowknife Bay independently of the larger approximations due to PLS modeling. ICA also represents the closest way to plot the internal variability of each member from point to point enabling us to discuss the internal variability in composition of each outcrop. In addition, hydrogen is not quantified by the PLS algorithm, whereas ICA plots enable the relative comparison of hydrogen with other elements.

4.1. Variations in Average Compositions

The PLS method was used to derive the compositions of individual laser shot locations of each target (see details in Appendix B). All individual targets were grouped to derive average compositions according to the stratigraphy described in previous sections in order to compare variations in chemistry with stratigraphy and texture. Data collected within the drill hole and on the brushed area of the Wernecke

Table 2. Standard Deviation in Oxides Weight Percent Around the Average Values Obtained in Table 1^a

Member	Outcrop	SiO ₂	TiO ₂	Al ₂ O ₃	FeO _T	MgO	CaO	Na ₂ O	K ₂ O	Total
	<i>RMSEP</i>	<i>7.1</i>	<i>0.55</i>	<i>3.7</i>	<i>4</i>	<i>3</i>	<i>3.3</i>	<i>0.7</i>	<i>0.9</i>	
Sheepbed	Full unit	3.3	0.2	0.9	1.2	1.4	1.0	0.3	0.2	4.9
Sheepbed	The Snake (dike)	3.2	0.1	0.8	2.0	1.1	1.4	0.3	0.3	6.2
Gillespie Lake	Full unit	3.3	0.3	1.0	1.7	1.7	1.2	0.4	0.3	5.7
Glenelg	Point Lake	5.6	0.3	2.3	2.5	1.6	1.9	0.8	0.6	7.2
Glenelg	Shaler	4.6	0.3	1.8	2.2	1.9	1.7	0.5	0.5	6.1
Glenelg	Rocknest	4.0	0.3	1.3	2.3	1.1	1.6	0.5	0.4	5.9
Glenelg	Bathurst	1.0	0.1	0.4	0.7	0.4	0.4	0.2	0.4	1.9
Layered floats		3.9	0.2	0.9	1.5	1.2	0.8	0.3	0.3	5.4
<i>Glenelg</i>	<i>Shaler layered</i>	<i>4.7</i>	<i>0.3</i>	<i>1.7</i>	<i>2.2</i>	<i>1.8</i>	<i>1.7</i>	<i>0.5</i>	<i>0.5</i>	<i>6.4</i>
<i>Glenelg</i>	<i>Shaler pitted</i>	<i>5.2</i>	<i>0.3</i>	<i>2.1</i>	<i>2.4</i>	<i>1.8</i>	<i>1.7</i>	<i>0.6</i>	<i>0.6</i>	<i>5.1</i>

^aThis value takes into account both the natural variability of the target and the precision of the method. RMSEP is the root-mean-square error of prediction and corresponds to the absolute accuracy of the PLS method based on the cross validation of 66 known composition. Standard deviations are far lower than the RMSEPs and can be used as a conservative value of the data precision (as it includes the natural point-to-point variability in grains chemistry and the technique precision, see Appendix B and *Blaney et al.* [2014], for more explanations). In italic, the two last rows split the Shaler outcrop in two distinct facies, the layered Shaler (usually nonpitted) and the pitted texture at Shaler.

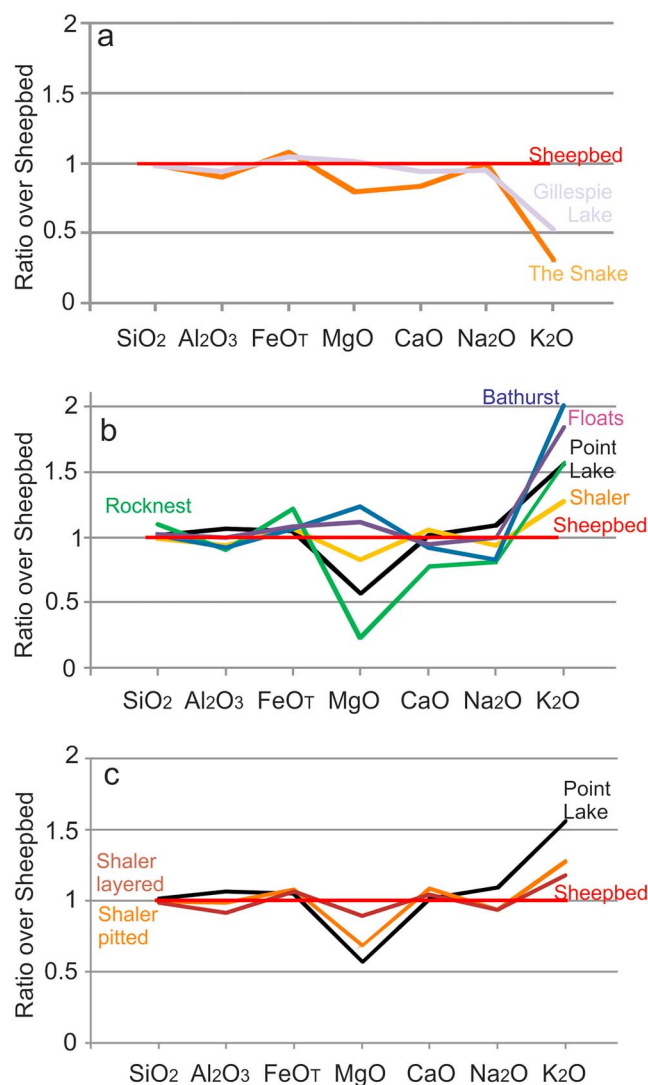


Figure 13. Plots of the average major element compositions of Yellowknife Bay members, including various Glenelg facies, normalized to the Sheepbed mean composition. (a) Average of all measurements in drill and brushed areas plotted together with Gillespie Lake and the Snake dike. (b and c) Plots of the various Glenelg outcrops. Note the high variability in Mg. See text for explanations.

target are presented separately, as are the Snake dike and the layered float rocks (Table 1). Deviations around the average values are primarily the result of natural variations in composition at the size of the laser beam, typically 200–600 μm , a size at which rocks start to display a variability in composition due to individual minerals. We thus choose not to plot the standard deviation of Table 2 in Figure 13, because this figure is intended to display the variations in the average bulk chemistry and not the variability in composition of all locations targeted. That variability is the subject of the ICA plots (section 4.2).

4.1.1. Comparison Between Sheepbed and Gillespie Lake Members

Gillespie Lake (Table 1) displays negligible differences in composition compared to the Sheepbed member mudstones despite the fact that the grain size is coarser. The Snake sedimentary dike is close to the Sheepbed composition as well but is depleted in Mg, Ca, and K, and slightly enriched in Fe. These differences are minor, especially given the fewer observations at the Snake (23 locations), but it could suggest an origin of the filling material in a distinct layer, such as in another layer below the observed Sheepbed member. In contrast, the Snake composition is clearly different from other rocks of the stratigraphic column (Table 1 and Figure 13a), showing that it did not form from a fracture filled during stages of deposition subsequent to that of the Gillespie Lake sand body.

4.1.2. Composition of the Glenelg Member at Point Lake and Shaler Outcrops

Shaler is slightly depleted in Mg and enriched in K compared to Sheepbed. Point Lake displays a similar trend to Shaler but with a stronger depletion in Mg and a stronger enrichment in Na and K. The overall comparison shows that the Shaler outcrop's composition matches closely that of Point Lake despite the apparent difference in textures (section 3.2). ChemCam spectra at individual Shaler and Point Lake locations (respectively, Steep Rock point 11 and Knob Lake points 1 and 5) suggest that the K enrichment is correlated with Si, Na, and Al (Figures 8 and 9). These trends suggest the presence of alkali feldspars in the form of coarse grains, which may explain the slight enrichment in alkali compared to Gillespie sandstones.

Based on their textures, a similarity was suggested between the pitted material at Shaler and the overall Point Lake facies (Figure 9b compared to Figures 3a and 8). For this reason, a distinct average has been calculated (Table 1) using the four targets analyzed from the pitted texture at the Shaler outcrop (e.g., at Steep Rock, see Appendix B). This particular average is plotted in Figure 13c. Compared to the nonpitted texture, the pitted texture at Shaler has a similar overall composition, but it displays a drop in Mg that brings it close to

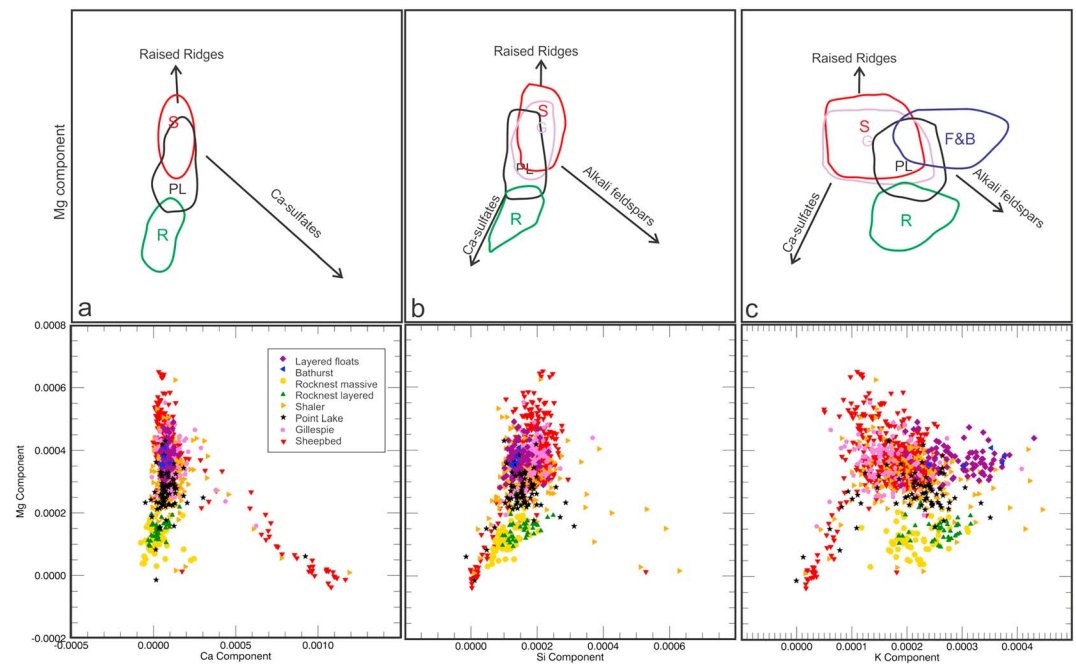


Figure 14. Independent Component Analysis (ICA) plots of the main outcrops of Yellowknife Bay, including the layered float rocks. An interpretative sketch is shown above for clarity. (a–c) Plots of Mg versus Ca, Si, and K. Ca-rich and Mg-rich diagenetic features plot in distinct directions. X and Y axes represent ICA scores of the component mentioned on the axis.

that of Point Lake. Within the Yellowknife Bay formation, this stronger depletion in Mg thus appears to be a property specific to Point Lake and the pitted texture observed at Shaler outcrop (see discussion).

4.1.3. Composition of the Glenelg Member at Rocknest and Bathurst Outcrops

Rocknest has a much different composition than Shaler and Point Lake, relative to Sheepbed or Gillespie Lake. Most major elements abundances are different from those of the other Glenelg outcrops. Rocknest is characterized by higher Fe, strongly depleted Mg, and lower Ca and Na, relative to the other Glenelg outcrops as well as the lower members. The composition of Rocknest appears therefore shifted, or perhaps disconnected, from the rest of the Yellowknife Bay formation.

Bathurst shows a distinct composition from all other members/outcrops, including Rocknest, its closest neighbor in terms of location (Table 1 and Figure 13b). Bathurst is the only outcrop that is enriched in Mg compared to Sheepbed and all the other selected areas. Bathurst also displays a strong enrichment in K that is not correlated with any Na enrichment. By comparison to other outcrops/members, the layered float rocks, which were averaged together, have very similar compositions to that of Bathurst (Table 1).

4.2. Composition of Individual Locations Analyzed by ChemCam Using ICA Plots

Various ICA plots were made for comparing the different members of the Yellowknife Bay formation, including the multiple facies observed in the Glenelg member (Figures 14–16). In these plots, diagenetic features (ridges and veins) were not removed from the database. For the readability of the plot, the Snake dike is not shown as it would plot over the Sheepbed and Gillespie members. The Rocknest outcrop is split into two parts corresponding to the massive boulders on one side and to the smooth layered rocks on the other side. The Glenelg members are thus divided into five groups of outcrops: Rocknest layered, Rocknest massive, Bathurst, Point Lake, and Shaler. An interpretative sketch is provided in parallel to the plot to provide an easier way to understand these observations. The ICA plots presented here are focused on elements that were identified to be of interest from the PLS averages: Mg, K, and Ti. No plot using Al is shown because this element did not provide distinctive variations.

4.2.1. Variability in Composition Within Given Members and Outcrops

The scattering in composition of the individual locations is visible on ICA plots. Points from Sheepbed and Gillespie members cluster together, with exception of Mg-enriched raised ridges and Ca-enriched sulfate

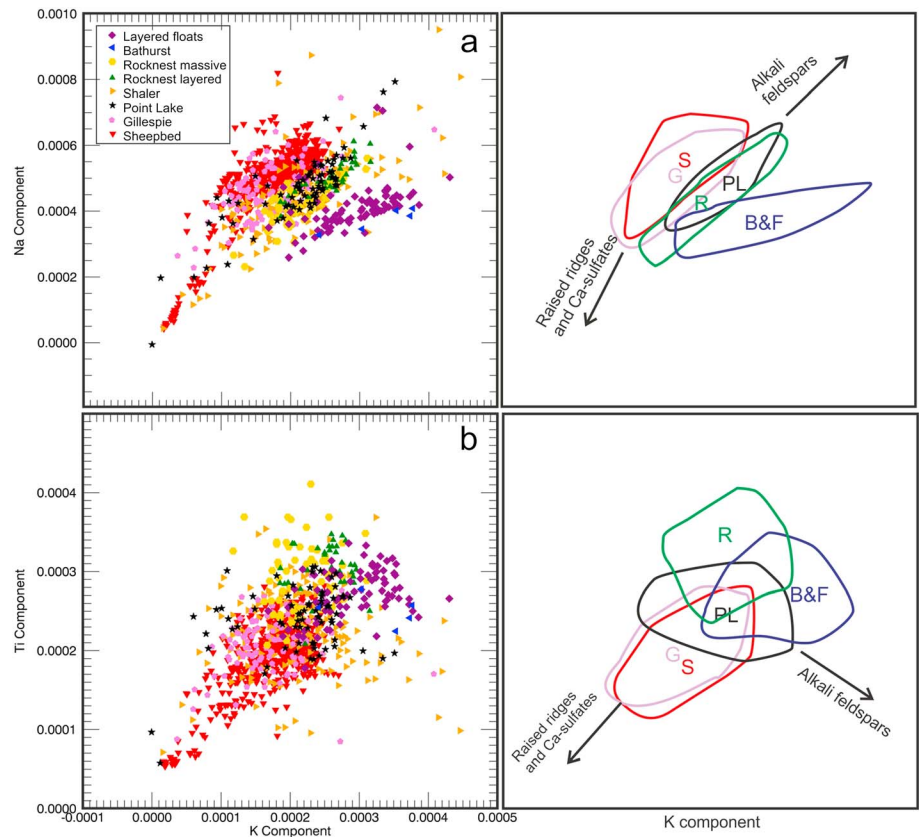


Figure 15. ICA plots showing K versus (a) Na and (b) Ti. Interpretative sketches are shown at right. Here diagenetic features plot together. The points showing enhanced Na and K correspond to alkali feldspars. Note the distinct K/Na ratio of the layered float rocks and Bathurst. X and Y axes represent ICA scores of the component mentioned on the axis.

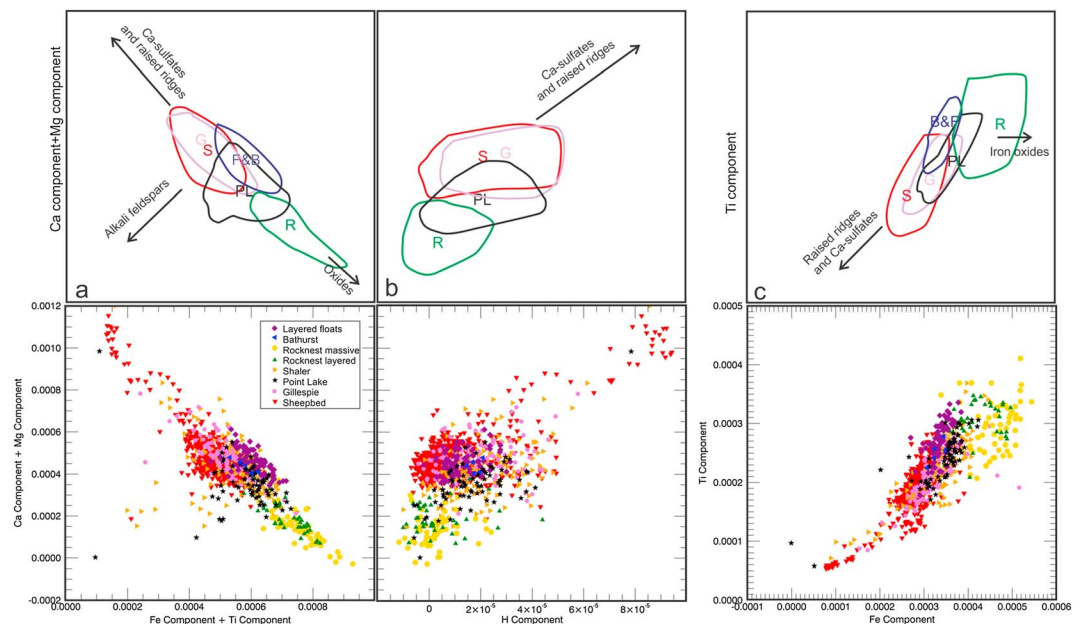


Figure 16. ICA plots showing (a) Ca + Mg versus Fe + Ti and (b) H, as well as (c) Fe versus Ti. Interpretative sketches are shown at right. Hydrogen variations should be taken with caution due to potential matrix effects from material of different physical properties. See text for explanations. X and Y axes represent ICA scores of the component mentioned on the axis.

veins and nodules (Figure 14). Series of points from Point Lake and Rocknest outcrops, and the float rocks, each form their own relatively tight clusters except for several outliers. Likewise, the float rocks usually plot together except for a few outliers. The Shaler outcrop, in contrast, displays a huge variability in the composition of the points in all graphs. Such a result is consistent with the fact that Shaler is a coarse to very coarse grained sandstone. Typical grain sizes of 1–2 mm are significantly larger than the laser beam diameter explaining this larger variability. For Shaler outcrop, the average bulk composition established from all locations using PLS will be more useful for cross comparisons between the different outcrops than ICA plots of individual locations. For this reason we did not divide Shaler into layered and pitted textures here. For the other members/outcrops, there is relatively good consistency between points grouped together, suggesting less compositional effects from the variability of grains due to their smaller sizes.

4.2.2. Cross Comparisons Using ICA Plots

The first series of plots show variations relative to Mg (Figure 14), an element that displays considerable variation in the normalized average plots (Figure 13). In all ICA plots, the Gillespie Lake member plots on top of or very close to the Sheepbed member. In the same way, float rocks and the Bathurst outcrop are grouped in the interpretative sketch because they plot together in all ICA graphs. The ICA plots confirm the relative trend observed in the average PLS measurements, with lower Mg at Point Lake outcrop compared to the Sheepbed and Gillespie Lake members. More specifically, the plots of Ca versus Mg (Figure 14a) allow us to distinguish those observations that correspond to Ca-sulfate veins and nodules as well as the raised ridges, the Mg enrichment of which is more limited than that of Ca in the sulfates. The plot in Figure 14b highlights the presence of a few Si-enriched points. It also suggests that the Rocknest outcrop may not be slightly enriched in Si as expected from the PLS result (Figure 13 and Table 1, this slight difference between PLS and ICA may be related to the lack of Fe-rich geostandards in the current PLS training set). The plot of K versus Mg is one of the most discriminating plots (Figures 14c). It confirms variations from the average PLS results, i.e., higher K for Bathurst and float rocks and intermediate K content for Point Lake and Rocknest outcrops.

The plot of K versus Na is important for understanding the provenance or diagenetic evolution of these sediments (Figure 15). This plot shows that the K/Na ratio is distinct for Bathurst (and layered float rocks) relative to all the other outcrops. Point Lake and Rocknest outcrops plot together in this graph, although on the other graphs they plot more or less separately. In the same way, the K versus Ti plot is useful for constraining the provenance and alteration of a target because Ti tends to be immobile relative to the more mobile element K. Nevertheless, the main deviation from the majority of points is only related to the higher K proportion of the Bathurst-layered float rock combined group.

Comparison of Ca + Mg versus Fe + Ti offers a way to distinguish oxide components and other minerals (Figure 16). The Rocknest outcrop plots show very strong Fe and Ti enrichments, distinct from other outcrops. On the Fe versus Ti plot (Figure 16c), Rocknest plots much more to the Fe side than the Ti side, suggesting this enrichment in the Fe + Ti plot is mainly driven by iron. On both plots (Figures 16a and 16c), the Point Lake outcrop is intermediate between Sheepbed and Rocknest outcrops. Nevertheless, the negative linear trend in Figure 16a is partly due to the effect of Fe and Ti depletion when having Ca + Mg enrichment due to Ca-sulfate veins and Mg-rich raised ridges.

Lastly, a plot showing Ca + Mg versus H (Figure 16b) is provided to discuss hydration. A strong hydrogen component is found for Ca-rich phases corresponding to the sulfate veins and nodules [Nachon *et al.*, 2014; Schröder *et al.*, 2014]. Most outcrops at Yellowknife Bay display hydrogen, although with varying levels. Assuming these variations are related to actual variations and not matrix effects, the Rocknest and Point Lake outcrops are the least hydrated of all outcrops analyzed. The Point Lake outcrop is more hydrated for the locations that are more Ca + Mg rich. Sheepbed and Gillespie Lake members have approximately the same hydration, perhaps slightly higher for the Gillespie Lake sandstone.

4.3. Summary of Results

Chemical variations observed by both PLS and ICA plots, and coupled to the different texture/facies of the Yellowknife Bay formation can now be summarized (Table 3 and Figure 17). First, the major element chemistry of Sheepbed and Gillespie Lake members is very similar, including the level of hydration. The lack of any significant difference that could be related to mechanical weathering or grain sorting (from a mudstone to a sandstone) or diagenetic chemical alteration (due to differences such as permeability) between the two members is striking and will be discussed in section 5.1.

Table 3. Summary of Observations and Interpretations on the Different Facies (in Stratigraphic Order From top to Bottom) Made in This Study and Including Previous Observations Made in *Grotzinger et al. [2014]*, *McLennan et al. [2014]*, *Anderson et al. [2014]*, and *Blaney et al. [2014]*

Stratigraphy	Texture	Chemistry	Interpretation
Glenelg member Bathurst	Faint layering, mm thick lamination. Siltstone to sandstone.	High K, distinct high K/Na ratio. Similar to layered floats found in hummocky plains.	Unknown origin. Unknown cementation. May not be part of Yellowknife Bay sediments. Extends away to the south.
Glenelg member Rocknest	Layered sandstone or massive texture with local flow features.	High Fe and alkali. Mg depleted. Similar composition of both textures.	Unknown depositional origin. Cement with Fe oxides. Disturbance by late event may explain the massive textures.
Glenelg member Shaler	Laminated sandstone with cross bedding, locally siltstone. Lateral variations with pitted texture.	Close to Sheepbed and Gillespie Lake composition except higher K connected to feldspars. Lower Mg in pitted texture.	Fluvial sediments. Local alteration during diagenesis forming pitted texture.
Glenelg member Point Lake	Pitted texture locally large vugs with glassy texture. Layering not obvious. Many cracks.	High alkali. Low Mg. Glassy texture contains points with high K, Na (likely feldspars)	Diagenetically modified sediments with enhanced alkali content and dissolution features.
Gillespie Lake member	Fine grained to pebbly sandstone. Strong induration, poor layering. Many cracks and filled veins.	Similar to Sheepbed. Unidentified hydrated phases in proportion as high as in Sheepbed.	Fluvial sediments. Cementation by aqueous fluids.
Sheepbed member	Local layering visible. Mudstone to siltstone. Many filled veins and open cracks	Homogeneous mafic composition except diagenetic features.	Lacustrine sediments. Early in situ diagenetic alteration. Late diagenetic episode with calcium sulfate veins.

Second, Point Lake and Shaler display compositions that are close to Sheepbed and Gillespie Lake for most elements, except higher K and lower Mg. The progressive transition of facies observed from Gillespie Lake to Point Lake (Figure 8g) points toward a common origin and evolution for all of these rocks despite their various textures and slight chemical differences. In more detail, Point Lake and Shaler display similar compositional trends as well, although presenting very different texture (resistant, massive, and pitted at Point Lake versus

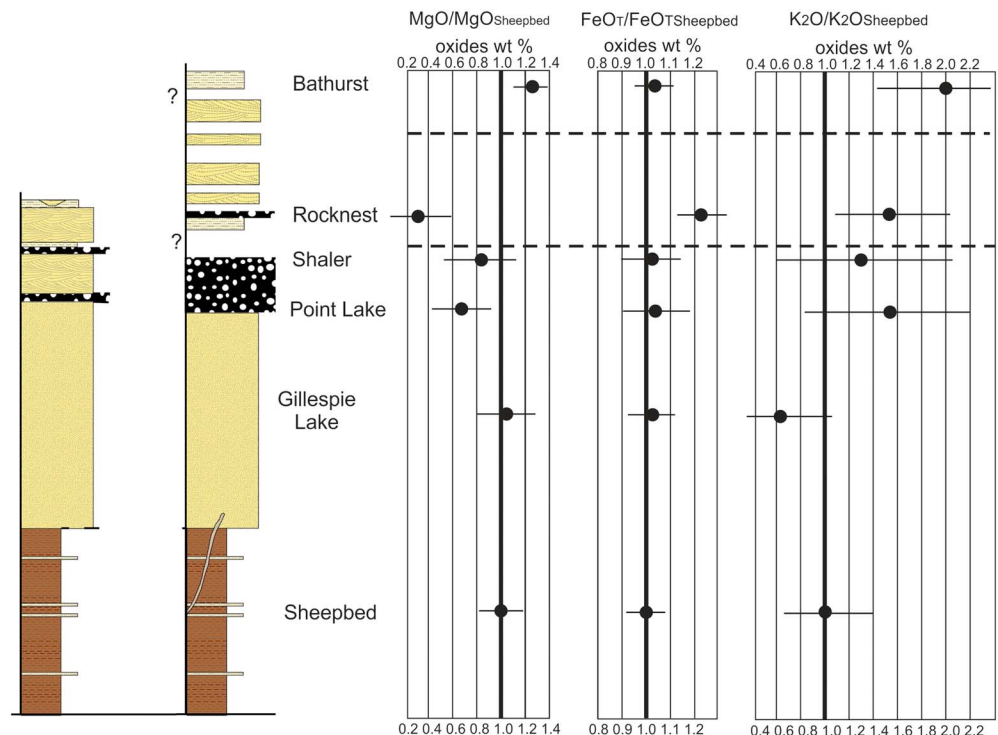


Figure 17. Chemostratigraphy of Yellowknife Bay showing, respectively, from left to right, the southern and northern stratigraphic section and three major elements of main interest: Mg, Fe, and K plotted in oxide wt %. Plots show relative variations from an average composition determined from the 480 points analyzed at Sheepbed. Horizontal bars represent the standard deviation around these average compositions corresponding both to the precision of the instrument and the natural variability in composition within each outcrop/member.

finely layered at Shaler). Furthermore, the targets with pitted texture at Shaler display the same depletion in Mg relative to the nonpitted layers of Shaler. These characteristics question the origin of the facies variation and the role of the pitted texture in the massive layers (see discussion in section 5.2).

Third, both Bathurst and Rocknest are strongly different in composition from sediments observed in lower part of the section. They are also distinct between themselves. In contrast, the chemistry on the two distinct facies of Rocknest (layered versus massive) is similar pointing toward a common origin. At Rocknest, the low amount of Mg and the high amount of Fe is not typical of enrichment in ferromagnesian minerals. The high Fe is also not directly correlated with enhanced Ti as it is frequently. By comparison, Bathurst displays the highest K content of the section. Bathurst and the layered float rocks plot together showing these floats likely originate from Bathurst layers. The similar K/Na ratios of these rocks and the difference from all other groups observed on the ICA plot (Figure 15) are significant. This outcrop also extends farther away on the hummocky plains from the unique location it has been analyzed in place (see discussion in section 5.3).

5. Implications and Discussions

5.1. The Cementation of the Gillespie Lake Sandstones

The Gillespie Lake member has a composition very close to that of the Sheepbed member mudstones, leaving few doubts about a common provenance. As Gillespie Lake likely represents an increase in energy to the depositional system with coarse-grained deposits [Grotzinger *et al.*, 2014], it may also contain the same fine-grained material that comprises the mudstones. A similar composition is therefore not surprising. Nevertheless, the presence of a significant hydrogen signal in the Gillespie sandstone at a level similar to, if not higher than in the Sheepbed mudstones (ICA plot in Figure 16b), suggests a significant proportion of hydrous minerals there too. The homogeneity of the rock at the laser ablation scale limits direct identification of the hydrous phase(s). It also does not help understand if these phases are present as cement, matrix, or sand grains. Nevertheless, hydrous minerals in sandstones are much more common as matrix or cement than as sand grains, because these minerals are more subject to abrasion and are generally not present as transported sand grains, as observed on Earth [e.g., Fowler and Yang, 2003; Garzanti *et al.*, 2007]. We thus consider two main hypotheses: a detrital origin forming a matrix of fine grains or an authigenic origin with hydrous minerals cementing the sandstones.

If the hydrous minerals at Gillespie Lake are detrital, this phase should also be present in the mudstones, which should have collected the same detrital grains. Mg smectites detected by CheMin at a proportion of ~20% [Vaniman *et al.*, 2014] are the main candidates for explaining this hydrous phase in the Sheepbed member. Yet the formation of these smectites within Sheepbed mudstones is explained by diagenetic processes [McLennan *et al.*, 2014]. If this interpretation is confirmed, a similar nature is therefore required for the sandstones as well, or we should observe another type of hydrous mineral in the mudstones that would correspond to those with a detrital origin, and contrary to the observation of a unique type of phyllosilicate in the mudstones. Mudstones are relatively impermeable compared to sandstones and contain small grains (<10–20 μm) that could be altered over short periods, defining an overall environment favorable for diagenetic alteration [e.g., Fowler and Yang, 2003]. We consider two hypotheses for the sandstones cementation. First, the Gillespie Lake member is located just above the Sheepbed member. During the Sheepbed mudstone diagenesis, mud deposits may have expelled fluids due to overpressure. The proximity of the Gillespie Lake sandstones may have helped to fill its pore space with Mg-enriched fluids, thus explaining the Gillespie Lake hydration level in this way. Second, cements could also have filled the pores later and could be linked to the variations in Mg observed in the overlying layers at Point Lake (see discussion in section 5.2). To conclude, we interpret the hydrous mineral phases indirectly identified by the hydrogen detected by ChemCam to be related to the cementation observed in the Gillespie Lake member.

5.2. Variability in Texture and Composition Between the Point Lake and Shaler Outcrops

The dark tone, rough texture and large number of voids at Point Lake could call into question its origin as part of the same depositional system. For instance, massive layers could be explained by a volcanic origin, but such an origin is unlikely due to the presence of coarse sand grains (Figure 8b), the lack of a sharp transition between Point Lake and the other units that are clearly sedimentary (Figure 8g), and the similarity in composition with the layers with pitted texture at Shaler, which are intimately interlayered with cross-bedded sandstones. ChemCam spectra at individual Shaler and Point Lake locations suggest that the K enrichment

indicates the presence of alkali feldspar grains in the material deposited (Figures 8 and 9), perhaps related to slight variations in the deposited material, with coarser grains preserved here than at Gillespie Lake.

We measure a lower Mg proportion in both outcrops. At the Shaler outcrop, the lower Mg is specifically observed in association with the pitted textures, whereas the surrounding beds do not show the same correlation. Voids and pits in such sediments are able to form either during the diagenetic history of the layers, for instance by dissolution, or during postexposure history from weathering. On Earth, coarse-grained sandstones can weather out as tafoni, polygonal cracks, or pits [e.g., *Chan et al.*, 2008], and these features often have regular shapes such as honeycomb or polygonal textures, unlike the pits observed here. Most voids at Point Lake are irregular and not associated with networks of cracks. The pitted layers are resistant to erosion, as shown at Point Lake, which forms a prominent outcrop. The transition from Gillespie Lake member to Point Lake outcrop (Figure 8g) suggests that the pitted texture is specific to this facies and does not correspond to modern weathering, though the latter process could locally have contributed to their enlargement. Voids and cracks are locally filled by light-toned material corresponding to calcium sulfates [*Nachon et al.*, 2014] but not as common as in Gillespie Lake and Sheepbed. Figure 8d shows one of these locations (white arrow, known as Measles Point in *Nachon et al.* [2014]). Figure 8e shows a 5 mm wide light-toned nodule (white arrow) inside a large void. This last observation shows that the sulfate-rich fluid precipitated in locations where the void was already present. A possible explanation of this sequence of events may be that the rock experienced dissolution to form the voids prior to the sulfur-rich fluid circulation and prior to further widening of these pits by more recent weathering at the surface. Mg is a mobile element which can be enriched in cements and diagenetic features, as observed in raised ridges of the Sheepbed mudstones [*Léveillé et al.*, 2014].

An important observation in the interpretation of this lower Mg is also that there is no significant difference in the relative abundance of Fe in the Point Lake and Shaler outcrops relative to the Gillespie Lake and Sheepbed members (Figure 17). A lower amount of Mg should be accompanied by a depletion of Fe as well if related to a lower proportion of some deposited phase. Mg could be depleted independently of Fe only if the difference was due to a phase that contained no Fe, for example, pure forsterite or enstatite. However, olivine minerals observed by CheMin at Gale crater (in Sheepbed mudstone and Rocknest sand dune) were relatively iron rich (Fo_{60}) and no pure enstatite was ever identified [*Blake et al.*, 2013, *Vaniman et al.*, 2014]. Relationships between facies and variations in Mg therefore suggest that this element varied inside these sediments due to fluid circulation, cementation, and subsequent dissolution of this cement rather than variations in provenance of the sediments.

5.3. Origin of the Rocknest and Bathurst Rock Outcrops

The Glenelg member displays a variety of textures and compositions that likely derived from various provenances, depositional modes or postdepositional processes, or some combination of these. Whereas Point Lake and Shaler outcrops differ only slightly from the Sheepbed and Gillespie Lake members, it is unclear whether the Rocknest and Bathurst outcrops are related to the same sedimentary assemblage or not.

The Rocknest outcrop has a totally different composition from all other studied rocks and is difficult to connect stratigraphically with the other facies due to burial of any possible contact [*Sumner et al.*, 2013]. We have found a similar composition on the two different textures (laminated versus massive). This observation suggests the possibility of postsedimentation modification such as mass flow or minor meteoritic impact. Chemically, the Rocknest outcrop is especially enriched in Fe and depleted in Mg and Ca relative to other facies. The enriched Fe is interpreted as representing a binding cement of iron oxides [*Blaney et al.*, 2014].

Bathurst's composition is different from the other studied outcrops as well and matches that of the layered float rocks analyzed along the traverse. The fine layering of Bathurst and of the layered float rocks suggests a very fine sandstone or a siltstone texture. The large laser ablation pits in most of them indicate a relatively soft material and confirm they correspond to sandstones/siltstones (or volcano-sedimentary tuffs) but not to lava flows in which laser excavation should be more limited (see *Arvidson et al.* [2014] for a discussion on laser ablation pits). Two of the layered float rocks, Kasegalik and Nullaktatok, were found ~100 m south-east of the other analyzed float rocks outside the Glenelg area (Figure 2). The similarity in texture and composition between layered float rocks and Bathurst targets allows us to infer that the Bathurst facies extends into

the hummocky plains bordering the Yellowknife Bay area to the southwest. More recent observations of K-rich rocks at Cooperstown (~sol 450) and Kimberley (~sol 650) may have a link to the Bathurst outcrop [Le Deit *et al.*, 2015].

Chemically, a unique aspect of Bathurst and the layered float rocks is the distinct K/Na ratio (Figure 15), which highlights variability in the provenance or possibly diagenesis. The fine-grained layering of Bathurst and layered float rocks suggests a sandstone or siltstone texture that could be interpreted as cemented eolian or fluvial deposits. Eolian material such as the Rocknest sand shadow is predominantly mafic and devoid of high K content [e.g., Blake *et al.*, 2013], suggesting this process is unlikely except by local reworking of K-rich rocks.

The K proportion is high (>1 wt % K_2O) compared to the average amount of the crustal K on Mars (0.45 wt % in average) [e.g., Taylor and McLennan, 2009]. A volcano-clastic origin is a possible alternative that may explain this distinct composition [Sautter *et al.*, 2013b; Schmidt *et al.*, 2014]. Physical sorting of ash deposits during the atmospheric transport can generate enrichments in K content, as observed on Earth [e.g., Lerbekmo and Campbell, 1969]. Although the texture may be eventually explained by eolian or fluvial processes, a contribution of ash in such deposits may be a possible explanation for the distinct chemistry. Lastly, hydrogen is present in these rocks (Figure 16b), suggesting a minor component of hydrated minerals that could constitute a cement, but no observation reveals correlated enrichments to identify such a cement, neither relate it to a higher K proportion. Therefore, explaining the K enrichment by fluid circulation remains speculative.

For both Bathurst and Rocknest outcrops, textural and compositional characteristics infer distinct processes relative to the rest of the Yellowknife Bay formation: both may have been deposited after the rest of the Yellowknife Bay formation, and potentially without having any genetic link with it, although no definitive answer can be given with regard to their detailed formation. If formed during the same fluvial deposition episodes, they indicate strong variations in the provenance that is beyond the goal of this study.

5.4. Implications for Mars Evolution

The role of water in the deposition and evolution of the Sheepbed lacustrine mudstones has been demonstrated from their facies and mineralogy [Vaniman *et al.*, 2014; Grotzinger *et al.*, 2014]. These results imply somewhat different climatic conditions for that epoch compared to the present climate [Vaniman *et al.*, 2014; Grotzinger *et al.*, 2014]. Our study shows in addition that the evolution was marked by fluid circulation in the overlying sandstones as well, as deduced by the role of Mg-rich fluids and the presence of significant hydration. These results may explain the cementation of sandstones overlying the lacustrine mudstones and demonstrate that early diagenetic processes were predominant in the evolution of the overall suite of sediments and not just for the Sheepbed mudstones in a lacustrine context. These results raise a question about the source and the nature of the aqueous activity subsequent to the presumably transient lacustrine activity in the Hesperian period.

The Peace Vallis fan is not unique on Mars: dozens of fans have been identified in impact craters and other settings [e.g., Moore and Howard, 2005; Grant and Wilson, 2011; Mangold *et al.*, 2012a]. A specific characteristic of the Peace Vallis fan is the high thermal inertia in the lower part of the fan [Anderson and Bell, 2010; Ferguson *et al.*, 2012]. This higher thermal material corresponds to the cemented sandstones and mudstones visited at Yellowknife Bay [Grotzinger *et al.*, 2014]. At Majuro crater, high-resolution thermal infrared images of the lower fan reveals a high thermal inertia and Fe/Mg smectites are detected with Compact Reconnaissance Imaging Spectrometer for Mars (CRISM) data [Mangold *et al.*, 2012b]. The similarity to the context at Gale—cemented lower fan and presence of clays—is striking. At Majuro, observations suggested the occurrence of hydrothermal circulation likely related to the impact crater's remnant heat [Mangold *et al.*, 2012b]. Hydrothermal circulation could be a source of diagenetic fluids at temperatures sufficient to produce chemical changes over a short duration. This hypothesis was considered as a possibility for explaining some observations at Gale crater [Newsom *et al.*, 2014] but may not fit the overall chronology of fluvial episodes, with Peace Vallis fan having developed relatively late in the evolution of the crater [Palucis *et al.*, 2014; Grant *et al.*, 2014]. In the absence of ground-based evidence for this hypothesis, a diagenetic environment resulting from burial and relatively low temperature fluids is more likely. The depth of burial and the temperatures required to provide diagenetic fluids to cement these sandstones remain unknown and are important parameters to constrain the chemical pathways. A better understanding of these postdepositional aqueous episodes are important to set up their context of formation, as the Hesperian is usually considered to be limited to short-term episodes and therefore has not been considered capable of prolonged aqueous alteration [e.g., Carter *et al.*, 2013].

6. Conclusions

Our study integrates data from the chemistry and textures of the Yellowknife Bay sediments to provide more inputs on the provenance and diagenetic evolution of these fluvial deposits (Table 3):

1. The new detection of hydrogen in the sandstones of Gillespie Lake demonstrates the presence of hydrous minerals, potentially in the same proportion than in the Sheepbed mudstones where they were identified as smectites [Vaniman *et al.*, 2014]. This observation suggests that smectites were also involved in the cementation of the sandstones during diagenetic evolution.
2. The lower section of the Glenelg member displays only slight chemical variations relative to the Sheepbed mudstone. The higher K content can be connected to the presence of alkali feldspars (at both Point Lake and Shaler), likely due to variation in the source material and/or a larger grain size distribution in these layers. Chemistry helped to show the genetic link between these outcrops of different textures from laminated to resistant massive layers. These outcrops display variations in Mg correlated with pitted textures that are interpreted as the result of diagenetic processes including cementation and subsequent dissolution.
3. The Glenelg member displays strong variations in composition in its upper section, at Rocknest and Bathurst_Inlet. These differences show a change in the depositional system compared to that responsible for depositing the underlying sediments, pointing, at least, to strong differences in the provenance of sediments. As a side note, the presence of float rocks found along the rover traverse with similar compositions to Bathurst_Inlet additionally demonstrate that these uppermost outcrops extend further away in the nearby hummocky plains.

Appendix A

Summary of ChemCam LIBS data included in the average composition of each member/outcrop plotted in Figure 11. Most observations use 30 laser shots to collect 30 spectra at the same location. The column "Points Removed" provides the location numbers for which the laser hit soils (S) or diagenetic features such as calcium sulfate veins (V) or raised ridges (RR). Locations for which laser coupling or focus were bad, or the quantification was misleading, were also removed (F). Only float rocks that were layered (as in Figure 10) were included. Most float rocks on the hummocky plains are not layered. Several targets in the YKB area were not included because of either poor quality or the presence of extended diagenetic features or soils (Asiak, Husky creek, Bonnet Plume of sol 166, Byng, Denault, Reddick Bight, Rapitan, Mc Grath2 of sol 184, Mc Grath of sol 189, Keskarah, Byng, Christopher Island, and Rowatt) or because they were too far (>5 m) for consistent PLS processing (Mehinek, Whishart, Wakham Bay, Discovery Creek, Long Island, and John Klein of sol 155).

Table A1. List of ChemCam Targets Used

Sol	Targets	Member/Outcrop	Number of Locations	Shots	Points Removed	Distance (m)
126	Sheepbed	Sheepbed	9	30		4.22
126	Beachrock	Sheepbed	9	30		3.27
127	Belcher	Sheepbed	9	30		3.80
129	Flaherty	Sheepbed	5	30		2.38
129	Richardson	Sheepbed	5	30		2.48
130	Flaherty_2	Sheepbed	5	30		2.38
130	Richardson_2	Sheepbed	5	30	V1, V2, and V4	2.50
130	Barn	Sheepbed	5	30		4.55
135	Rackla	Sheepbed	9	30		2.41
149	Bonnet_Plume	Sheepbed	9	30	S6 and S7	3.45
150	Haig	Sheepbed	5	30		3.94
150	Hay_Creek	Sheepbed	9	30		2.92
150	Hayhook	Sheepbed	9	30	V4	3.21
150	Hudson_Bay	Sheepbed	9	30		3.37
151	Quartet	Sheepbed	9	30	V7	4.25
152	Hay_Creek_new	Sheepbed	9	30		2.56
152	Quartet_new	Sheepbed	9	30	V7	3.79
154	Selwyn	Sheepbed	10	30	V8 and V9	3.19
157	Selwyn_1	Sheepbed	20	30	V14 and V15	3.17

Table A1. (continued)

Sol	Targets	Member/Outcrop	Number of Locations	Shots	Points Removed	Distance (m)
157	Selwyn_2	Sheepbed	5	30	V3 and V5	3.20
159	Selwyn_DP	Sheepbed	4	150	V1	3.23
160	Nastapoka	Sheepbed	9	30		3.25
160	Mavor	Sheepbed	9	30	V5 and V6	3.18
164	Cape_Smith	Sheepbed	9	30		4.33
164	Kootenay	Sheepbed	9	30		2.97
165	John_Klein_RP2	Sheepbed	9	30	RR2 and RR6	2.97
165	John_Klein_RP3	Sheepbed	9	30	RR4–RR7	2.97
165	Tukarak	Sheepbed	9	30	V2, V4, and V7	2.42
166	DT_RP5_STG	Sheepbed	5	30		3.42
166	DT_RP6	Sheepbed	5	30	V2	3.61
172	Wernecke_1	Sheepbed (brushed)	9	30		2.47
176	Gog	Sheepbed	9	30	S3, S6, and S9	2.56
183	Wernecke_2	Sheepbed (brushed)	9	30		2.47
187	Cumberland	Sheepbed	16	30		2.59
187	Seward_1	Sheepbed	16	30	V1–V6	2.31
188	Fury	Sheepbed	9	30	V6	2.26
188	Kazan	Sheepbed	25	30	V6 and V16	2.53
189	Iqqittuq	Sheepbed	9	30		2.43
189	Rae	Sheepbed	9	30		2.26
192	Bylot	Sheepbed	9	30		2.29
192	Rae	Sheepbed	9	30		2.26
193	McGrath_3	Sheepbed	10	30		2.27
195	Thelon	Sheepbed	9	30		3.03
226	Mc Grath_4	Sheepbed	20	30	RR4 and RR14–RR16	2.27
227	Drillhole	Sheepbed	10	30	V7, V9, S8, and S10	2.46
		(John Klein drill)				
232	Ruth	Sheepbed	25	30	V11, V12, V19, V22, and V23	2.78
234	McGrath_5	Sheepbed	5	150	RR1–RR3	2.26
274	Cumberland_CCAM	Sheepbed	5	30		2.87
274	Kazan_CCAM	Sheepbed	5	30		2.89
275	Cumberland_Bowl	Sheepbed	9	30	V3	2.36
275	Cumberland_3	Sheepbed	9	30	V1, V3, and V9	2.34
284	CumberlandA_LL	Sheepbed (Cumberland drill)	10	30	F1	2.37
290	Lady_Nye_4	Sheepbed	15	30		2.43
292	Cumberland_3	Sheepbed	9	30	V2	2.35
292	Cumberland_4	Sheepbed	9	30		2.26
292	Duluth	Sheepbed	5	100		2.66
292	Sibley	Sheepbed	5	100		2.57
298	Cape Strawberry	Sheepbed	9	30		2.54
298	Mesabi	Sheepbed	9	30		2.29
147	Snake river	Snake dike	5	30		4.45
151	Little_Dal	Snake dike	9	30		3.81
151	Redstone	Snake dike	9	30		3.01
122	Kikerk	Gillespie Lake	5	30		2.59
124	Kahochella	Gillespie Lake	5	30		3.54
125	Crest	Gillespie Lake	9	30	V1 and V9	3.02
133	Gillespie_Lake_1	Gillespie Lake	9	30		2.48
133	Gillespie_Lake_2	Gillespie Lake	9	30	V3	2.55
151	Laddie	Gillespie Lake	9	30		3.21
157	Kipalu	Gillespie Lake	9	30	S1 and S5	3.36
169	Lucas_Creek	Gillespie Lake	5	30	V3	3.18
176	Nanok	Gillespie Lake	9	30	S2	2.77
181	Joliffe	Gillespie Lake	9	30		3.82
184	Nanok2	Gillespie Lake	10	30		2.78
186	Doublet	Gillespie Lake	10	30		2.79
186	Mugford	Gillespie Lake	5	30		3.47
283	Sulky_CCAM	Gillespie Lake	1	50		3.16

Table A1. (continued)

Sol	Targets	Member/Outcrop	Number of Locations	Shots	Points Removed	Distance (m)
104	Acasta	Point Lake	9	30		3.58
111	Amagok	Point Lake	5	30		3.78
113	Bell_Island	Point Lake	9	30	V1 and S3	2.28
116	Ingraham	Point Lake	9	30		4.55
123	Kapvik	Point Lake	9	30		4.37
302	Knob Lake	Point Lake	9	30	F1	4.74
302	Athole point	Point Lake	9	30		4.71
303	Balboa	Point Lake	9	30		2.24
304	LeRoux	Point Lake	9	30		3.98
305	Measles_Point	Point Lake	9	30	V9	2.25
305	Balboa_2	Point Lake	9	30		2.24
305	Nancroix	Point Lake	5	30		2.83
305	Croteau	Point Lake	10	30	F6–F10	2.30
121	Port_Radium_1	Shaler	5	30		3.13
121	Stanbridge	Shaler	5	30		3.90
309	Rove	Shaler	20	30		3.80
309	Ramah	Shaler	5	30		3.82
311	Michigamme	Shaler	20	30		4.03
311	Piling	Shaler	9	30		3.86
315	Gogebic	Shaler	9	30		3.30
315	Saglek	Shaler	9	30		2.47
316	Rusty_Shale	Shaler	10	30		4.68
317	Montaigne	Shaler	16	30		2.26
317	Double_Mer	Shaler	9	30	S1–S3, S5, and S6	2.78
319	Aillik	Shaler	9	30		2.45
319	Equalulik	Shaler (Pitted)	9	30		2.62
319	Cartwright	Shaler (Pitted)	6	30		3.11
322	Fabricius_Cliffs	Shaler	5	30		3.95
323	Steep_Rock	Shaler (Pitted)	20	30	F11	3.00
323	Camp_Island	Shaler	5	30		2.26
324	Howells	Shaler (Pitted)	25	30		2.26
57	Rocknest3	Rocknest layered	5	30		3.67
61	Pearson	Rocknest massive	9	30		3.58
68	Pearson_1	Rocknest massive	9	30		3.64
70	Snare	Rocknest massive	5	30		2.85
71	Rocknest_6	Rocknest massive	9	30		2.61
71	Peg	Rocknest layered	9	30		3.72
71	Zephyr	Rocknest massive	9	30	S1–S3 and S7–S9	2.65
77	Rocknest3_DP	Rocknest layered	1	600		3.44
77	Pearson_DP	Rocknest massive	1	600		3.64
79	Pearson2	Rocknest massive	9	30		3.62
79	Walsh	Rocknest massive	9	30		4.45
82	Rocknest3_1	Rocknest layered	10	30		3.47
82	Rocknest3_2	Rocknest layered	10	30		3.45
88	Rocknest6a	Rocknest massive	9	30		2.57
88	Rocknest6b	Rocknest massive	9	30		2.62
90	Rocknest__3_top1	Rocknest layered	25	30	S16 and S21–S25	3.48
55	Bathurst_CCAM_raster	Bathurst	5	30		2.51
111	Duncan_Lake	Float	24	30	F3–F6 and F15	2.85
114	Patterson_Lake	Float	10	30	S7	3.28
114	Jackson_Lake	Float	9	30		3.21
116	Duncan_Lake_vertical_start	Float	10	30		3.16
116	Kiwi lake	Float	9	30		4.47
117	Jackson_Lake_2	Float	5	30	S1 and S3	3.28
117	Jackson_Lake_3	Float	5	30		3.21
326	Chantrey	Float	25	30		3.68
329	Thomson	Float	10	30		2.73
335	Kasegalik	Float	5	30		3.88
336	Nullataktok	Float	5	30		2.85

Appendix B: Summary of Partial Least Square (PLS) Method and Results

Two data reduction methods were used in this work: Independent Component Analysis (ICA) and Partial Least Squares (PLS). ICA defines a generative model for the observed multivariate data, which is typically given as a large database of samples. In the model, the data variables are assumed to be linear mixtures of some unknown latent variables, and the mixing system is also unknown. The latent variables are assumed to be non-Gaussian and mutually independent and are referred to as the independent components of the observed data. These independent components, also called sources or factors, can be found by ICA. Statistical independence implies an absence of correlation, but is a more stringent condition: it means that the distribution of one variable does not tell anything about the distribution of the other variables. More explicitly, ICA defines a transform:

$$X = AS$$

where X represents the data, S the independent components, and A is the matrix of mixing coefficients. ICA identifies the products of $A^* S$ from X , but not A and S alone. The returned components are ordered according to a non-Gaussian parameter, rather than according to their contributions to the data. ICA is very robust to random noise in the data, which can be considered Gaussian. Applications of ICA to data such as LIBS spectra are more precise and easier to interpret than principal component analysis [Forni *et al.*, 2013a, 2013b].

PLS compares spectra to known standards analyzed in a test bed on Earth [Clegg *et al.*, 2009]. In a variation of this method, PLS1, the number of components can be predicted separately for each element [Clegg *et al.*, 2009] rather than having all elements determined simultaneously. This method allows different sets of standards to be used for determining the abundances of different elements. The first shots (1 to 5) show a clear contamination by dust [Meslin *et al.*, 2013; Lasue *et al.*, 2013]. Thus, to obtain average spectra representing the dust-free rock only, the last 25 shots are used.

Given the spectrum of an unknown target, PLS is used to determine the major element abundances that produced the spectrum, providing a reliable estimate of the target composition, assuming that it is within the compositional range of the training set [Wiens *et al.*, 2013]. Note that the laser destroys all molecular bonds, and no emission corresponding to minerals present in rocks can be identified directly. Molecular emissions are nevertheless present when recombination of atoms occur as the plasma cools [Gaft *et al.*, 2014; Forni *et al.*, 2014], and these molecules do not necessarily correspond to molecules that were present in the rock.

The PLS-derived abundances currently have sizeable absolute accuracy errors due to the limited compositional diversity of the training set spectra acquired on standards in lab and to the intrinsic variations in LIBS emissions [Cremers and Radziemski, 2006]. Errors estimated from tests in the lab, usually taken as root-mean-square error of prediction (RMSEP), currently vary significantly for the given elements, which in some cases can be critical for determining the rock class. The RMSEP describes the mean accuracy of the measurements over the whole training set. The accuracy is measured by leaving one standard out of the model, using this model to predict the composition of the standard that was removed, and determining the error, and so on for all standards [e.g., Wiens *et al.*, 2012, 2013]. Work is being completed on an expanded training set increasing the number of standards from 66 to > 350.

An issue that affects the quantification is that of the variable distance between the laser source and the sample [Cremers and Radziemski, 2006]. The distance has only a limited effect on much of the ChemCam LIBS data taken on Mars to date due to the fact that much of the data are taken relatively close to 3 m, and that is the distance at which the spectra were taken in the current training set. To reduce the effects of distance between the laser and the rock to analyze, only those targets that are within 2.2 m and 5 m have been considered in this study. The various distances of the targets are listed in Appendix A. In addition, the small size of the laser beam introduces a natural variability related to the mineralogical variations of rocks at the several hundred micrometers grain size, as discussed in section 2.1.

To give a notion of the variability of the PLS data of individual targets, the table below presents the results of the four targets representing Sheepbed, Gillespie Lake, Point Lake, and Shaler, the brushed target Wernecke shown in Figure 6b, and Bathurst shown in Figure 11. These data show the slight variability of the composition in Gillespie Lake and Sheepbed, except points on soils and veins that are removed for the averages. The data also show the larger chemical variability in Shaler and Point Lake. To avoid limitations due to this variability, averages were calculated on statistically large numbers of points for each outcrop.

Table B1. PLS Results Giving Elementary Chemistry in Weight Oxides Percents for Selected Targets to Give a Notion of the Point-to-Point Variability in Composition^a

Target Name	SiO ₂	TiO ₂	Al ₂ O ₃	FeO _T	MgO	CaO	Na ₂ O	K ₂ O	Total
RMSEP (see text above)	7.1	0.55	3.7	4	3	3.3	0.7	0.9	
Wernecke point 1	46.7	1.18	8.4	16.5	5.4	5.1	2.2	0.8	86.2
Wernecke point 2	45.8	1.05	8.3	16	5.6	6.8	2.6	0.9	87
Wernecke point 3	48.2	1.03	8.6	16.2	5.7	6.3	2.6	0.8	89.6
Wernecke point 4	45.6	1.04	8.2	14.8	5.7	5.9	2.6	1	85
Wernecke point 5	47.6	0.93	8.4	15.8	5.9	6.3	2.8	0.9	88.6
Wernecke point 6	44.6	0.89	7.9	15.7	5.8	6	2.5	0.9	84.1
Wernecke point 7	47.3	1.07	8.5	16.6	5.8	5.9	2.6	1	88.8
Wernecke point 8	47.6	1.03	8.4	16.1	6	6.4	2.5	0.8	88.8
Wernecke point 9	45.7	0.94	8.3	15.8	5.6	6.4	2.5	0.7	85.9
Average Wernecke, all points	46.6	1.01	8.3	15.9	5.7	6.1	2.5	0.9	87.1
Standard deviation	1.2	0.08	0.2	0.53	0.2	0.5	0.2	0.1	1.9
DT_RP6 point 1	51.5	0.97	9.2	17.1	8.7	6.6	2.5	0.5	97.1
DT_RP6 point 2	28.9	0.08	4.7	9.5	6.6	23.5	1.7	0	74.5 ^b
DT_RP6 point 3	56	0.74	8.7	17.2	9.7	6.5	2.9	0.6	102.3
DT_RP6 point 4	52.8	1.07	9.2	16.9	7.3	6.8	2.5	0.7	97.2
DT_RP6 point 5	51.1	1.11	8.9	17.5	7.1	6.1	2.5	0.8	95
DT_RP6 average (without point 2)	52.8	0.97	9	17.2	8.2	6.5	2.6	0.7	97.9
Standard deviation	2.2	0.17	0.2	0.2	1.2	0.3	0.2	0.1	3.1
Kipalu point 1	36.9	0.99	6.7	13.5	7	9.9	2.1	0	76.2 ^c
Kipalu point 2	42.5	1.02	7.1	17.9	7.7	5.1	1.9	0	82.8
Kipalu point 3	45.3	1.12	8.6	16.1	5.8	6.7	2.2	0	85.7
Kipalu point 4	44.7	0.79	8.1	16.3	6.1	5.6	2.8	0.2	84.6
Kipalu point 5	38.8	0.87	5.3	15.2	10.2	9.5	2	0	80.9 ^c
Kipalu point 6	46.6	1.22	7.8	17.7	7.8	6.5	2.1	0	89.6
Kipalu point 7	45.2	0.94	7.3	16.8	6.9	6.2	2.1	0	85.5
Kipalu point 8	42.7	1.03	7.7	16.7	6.3	5.7	2.1	0	82.1
Kipalu point 9	46.6	0.82	6.9	17.2	9.2	4.6	2.6	0.5	88.3
Kipalu average (without points 1 and 5)	44.8	0.99	7.6	17.0	7.1	5.8	2.3	0.1	85.5
Standard deviation	1.7	0.15	0.6	0.67	1.2	0.8	0.3	0.2	2.7
Knob Lake point 1	d	d	d	d	d	d	d	d	d
Knob Lake point 2	53.1	1.13	9.9	21.5	2.2	4.5	2.8	1.4	96.5
Knob Lake point 3	51.1	1.02	9.4	19.5	3.6	6.2	3	1.1	94.9
Knob Lake point 4	43.7	1.7	8.9	19.7	4.7	10.6	2.1	0.2	91.7
Knob Lake point 5	60.2	0.2	17.4	14	0	1.7	4.2	3.3	100.1
Knob Lake point 6	47.8	1.13	7.3	20.2	4.2	5.4	2.4	0.5	88.9
Knob Lake point 7	54.7	0.75	11.4	19.4	3.2	6.2	3.2	1.7	100.6
Knob Lake point 8	57.8	0.64	11.9	20	1.3	4.6	3.6	1.7	101.7
Knob Lake point 9	47.6	1.07	8.1	17.5	4.6	7.8	2.6	0.9	90.2
Knob Lake average, all points (except point 1)	52	0.95	10.5	19	3	5.9	3	1.3	95.6
Standard deviation	5.6	0.44	3.2	2.3	1.7	2.6	0.7	0.9	5.0
Steep_Rock point 1	43.4	0.99	7	19.5	5.4	7	2.1	0.4	85.8
Steep_Rock point 2	47.5	0.99	8.7	17.7	3.5	8	2.1	0.9	89.3
Steep_Rock point 3	41.2	1.04	6.2	18.3	6.1	7.5	1.9	0	82.1
Steep_Rock point 4	45.5	1.04	8.2	20	3.1	8.4	2.2	0.6	89
Steep_Rock point 5	44.7	0.98	7.1	19.9	4.8	6.5	2.2	0.7	87
Steep_Rock point 6	43.1	1.15	7.6	20.9	3	7	2.3	0.6	85.8
Steep_Rock point 7	44.6	1.08	7.5	20.6	4	7.1	2	0.6	87.5
Steep_Rock point 8	48.3	0.93	7.6	20.8	5	5.8	2.4	0.8	91.6
Steep_Rock point 9	45.4	1.1	7.7	18.8	4.9	10.1	2.5	0.3	90.9
Steep_Rock point 10	40.5	1.04	7.5	15.2	6.1	10.5	2.4	0.4	83.6
Steep_Rock point 11	67.1	0.24	17.1	11.3	0.5	3.5	4.6	2.9	107.2 ^d
Steep_Rock point 12	42	1.07	7.2	20.6	4.9	6.3	2.2	0	84.3
Steep_Rock point 13	43.6	0.87	6.9	19.6	5.4	6.1	2.1	0.3	84.9
Steep_Rock point 14	43.9	0.64	7.2	17.7	5.7	7.5	2.3	0.5	85.4
Steep_Rock point 15	45.6	0.92	8.5	18.7	3.5	7.6	2.4	0.4	87.6

Table B1. (continued)

Target Name	SiO ₂	TiO ₂	Al ₂ O ₃	FeO _T	MgO	CaO	Na ₂ O	K ₂ O	Total
Steep_Rock point 16	43	0.9	6.7	20.1	4.1	6	2.2	0.5	83.6
Steep_Rock point 17	44.9	0.95	7.1	18.3	5.8	6.7	2	0.7	86.5
Steep_Rock point 18	44.3	1.33	7.9	21.2	3.9	5.9	2.3	1	87.7
Steep_Rock point 19	49.2	1	9.2	18	2.3	8.2	2.5	1.5	91.9
Steep_Rock point 20	48.2	0.75	7.3	18.7	4	5.7	2.4	1	88.1
Average, all points (without point 11)	44.7	0.99	7.5	19.2	4.5	7.3	2.2	0.6	87.0
Standard deviation	2.4	0.15	0.7	1.5	1.1	1.3	0.2	0.4	2.8
Bathurst inlet point 1	45.2	1.48	6.8	18.4	7.5	5.5	1.6	0.6	87
Bathurst inlet point 2	46	1.53	7.7	17.6	7.1	6.4	2	1.3	89.6
Bathurst inlet point 3	47.1	1.34	7.3	17	8.2	6.0	2.2	1.4	90.5
Bathurst inlet point 4	47.9	1.52	7.8	18.1	7.5	5.6	2.1	1.5	91.9
Bathurst inlet point 5	46.9	1.64	7.6	18.8	7.5	5.7	1.8	0.9	91
Average, all points	46.6	1.50	7.4	18.0	7.6	5.8	1.9	1.1	90.0
Standard deviation	1.0	0.11	0.4	0.7	0.4	0.4	0.2	0.4	1.9

^aValues in bold correspond to the average of several points on the same target. Values in italic correspond to a point with too high total to be included in the average of this target.

^bIndicates a low total for which sulfur has been detected in abundance corresponding to the identification of calcium sulfates.

^cIndicates point in the soils, not in rocks targeted.

^dIndicates points for which PLS modeling overestimates the total, such as the case for pure feldspar minerals (note that the mineral identification is done using the individual spectra, not the quantitative data). The point 11 at Steep Rock has an overestimated total for the same reason. These points are not frequent and are not taken into account in averages.

The standard deviation on homogeneous targets (such as Wernecke, DT_RP6 without the sulfur-rich point, or Bathurst) can account for a conservative estimate of the precision of the measurements. Averages are calculated for each target using all points, and when applicable, by removing outliers not corresponding to the rock of interest (points on soil, veins, etc.). The standard deviation around the calculated average is usually much lower than the RMSEP of the corresponding elements (Table 2). For instance, for the 480 locations sampled in the Sheepbed unit, the standard deviation is $\pm 3.4\%$ around the mean value of 46.2% for SiO₂, and $\pm 1\%$ around the value of 6.3% for CaO, well below the RMSEP values. Deviations around the average values are primarily the result of natural variations in composition at the size of the laser beam, typically 200–600 μm , a size at which rocks start to display a variability in composition due to individual minerals, as well as the variability of rock composition from one point to another. As this manuscript displays mainly relative variations between different units, the precision (obtained by the standard deviation) will be a more adequate parameter than the accuracy (RMSEP).

The major element totals derived by PLS are frequently below 100%. This is largely because the PLS model does not take into account all elements, omitting volatile elements such as sulfur, phosphorus, chlorine, fluorine, as well as hydrogen. These phases may account for the missing fraction and PLS models, including additional elements that are underdevelopment.

We choose to normalize the elemental variations to the lacustrine Sheepbed mudstone because it plays the role of a reference deposit in the Yellowknife Bay series (Table 1). The other advantage of comparing compositions with Sheepbed is that the 480 ChemCam observation points guarantee good statistics for the average Sheepbed composition. Another option could have been to normalize the composition to the mean Martian crust, which has been estimated using APXS and Gamma-Ray Spectrometer measurements [e.g., Taylor and McLennan [2009]]. We choose not to use the Martian crust average as reference because the differences between members are rather subtle and better visible, taking the well-studied Sheepbed mudstones as reference.

References

- Anderson, R. B., and J. F. Bell (2010), Geologic mapping and characterization of Gale Crater and implications for its potential as a Mars Science Laboratory landing site, *Mars*, 5, 76–128, doi:10.1555/mars.2010.0004.
- Anderson, R. B., et al. (2014), ChemCam compositional results from the Shaler outcrop in Gale Crater, Mars, *Icarus*, doi:10.1016/j.icarus.2014.07.025.
- Arvidson, R. E., et al. (2014), Terrain physical properties derived from orbital data and the first 360 sols of Mars Science Laboratory Curiosity rover observations in Gale Crater, *J. Geophys. Res. Planets*, 119, 1322–1344, doi:10.1002/2013JE004605.

Acknowledgments

We acknowledge the helpful reviews of anonymous reviewers. Support for development and operation of the ChemCam instrument was supported in France by funds from the French Space Agency, Centre National d'Etudes Spatiales (CNES). Support was also received from INSU/CNRS and from OSUNA (Observatoire des Sciences de l'Univers de Nantes Atlantique). Support for development and operation in the U.S. was provided by NASA to the Mars Exploration Program and specifically to the MSL Team. Imaging and chemical data presented here are available in the NASA Planetary Data System (PDS) <http://pds-geosciences.wustl.edu/mis-sions/msl>. We are grateful to the MSL engineering and management teams (and especially the Jet Propulsion Laboratory, California Institute of Technology, under contract with NASA) for making the mission and this scientific investigation possible and to science team members who contributed to mission operations.

- Bell III, J. F., M. C. Malin, M. A. Caplinger, M. A. Ravine, A. S. Godber, M. C. Jungers, M. S. Rice, and R. B. Anderson (2012), Mastcam multispectral imaging on the Mars Science Laboratory rover: Wavelength coverage and imaging strategies at the Gale Crater field site. 43th *Lunar Planet. Sci. Conf.* abstract 2541.
- Blake, D. F., et al. (2013), Curiosity at Gale crater, Mars: Characterization and analysis of the Rocknest sand shadow, *Science*, *341*, doi:10.1126/science.1239505.
- Blaney, D. L., et al. (2014), Chemistry and texture of the rocks at "Rocknest," Gale crater: Evidence for sedimentary origin, *J. Geophys. Res. Planets*, *119*, 2109–2131, doi:10.1002/2013JE004590.
- Carter, J., F. Poulet, J.-P. Bibring, N. Mangold, and S. L. Murchie (2013), Hydrous minerals on Mars as seen by the CRISM and OMEGA imaging spectrometers: Updated global view, *J. Geophys. Res. Planets*, *118*, 831–858, doi:10.1029/2012JE004145.
- Chan, M. A., A. Yonkee, D. I. Netoff, W. M. Seiler, and R. L. Ford (2008), Polygonal cracks in bedrock on Earth and Mars: Implications for weathering, *Icarus*, *194*, 65–71.
- Clegg, S. M., E. Sklute, M. D. Dyar, J. E. Barefield, and R. C. Wiens (2009), Multivariate analysis of remote laser-induced breakdown spectroscopy spectra using partial least squares, principal component analysis, and related techniques, *Spectrochim. Acta B*, *64*, 79–88.
- Comon, P. (1994), Independent component analysis, a new concept?, *Signal Process.*, *36*, 287–314.
- Cousin, A., et al. (2014), Compositions of sub-millimeter-size clasts seen by ChemCam in Martian soils at Gale: A window into the production processes of soils, *Icarus*, *249*, 22–42, doi:10.1016/j.icarus.2014.04.052.
- Cremers, D. A., and L. J. Radziemski (1983), Detection of fluorine and chlorine in air by laser-induced breakdown spectroscopy, *Anal. Chem.*, *55*, 1252–1256.
- Cremers, D. A., and L. J. Radziemski (2006), *Handbook of Laser-Induced Breakdown Spectroscopy*, 292 pp., Wiley, San Francisco, Calif.
- Dehouck, E., N. Mangold, S. Le Mouéléc, V. Ansan, and F. Poulet (2010), Ismenius Cavus, Mars: A deep paleolake with phyllosilicate deposits, *Planet. Space Sci.*, *58*(6), 941–946.
- Dromart, G., C. Quantin, and O. Broucke (2007), Stratigraphic architectures spotted in southern Melas Chasma, Valles Marineris, Mars, *Geology*, *35*(4), 363–366, doi:10.1130/G23350A.1.
- Edgett K. S., et al., (2013), Curiosity's Mars Hand Lens Imager (MAHLI): Initial observations and activities. 44th *Lunar Planet. Sci. Conf.*, abstract 1199.
- Ferguson, R. L., P. R. Christensen, M. P. Golombek, and T. J. Parker (2012), Surface properties of the Mars Science Laboratory candidate landing sites: Characterization from orbit and predictions, *Space Sci. Rev.*, *179*, 739–773, doi:10.1007/s11214-012-9891-3.
- Forni, O., et al. (2013a), Chemical variability and trends in ChemCam Mars Observations in the first 90 sols using independent component analysis, 44th Lunar and Planetary Science Conference, held March 18–22, The Woodlands, Texas. LPI Contribution No. 1719, p.1262.
- Forni, O., S. Maurice, O. Gasnault, R. C. Wiens, A. Cousin, S. M. Clegg, J.-B. Sirven, and J. Lasue (2013b), Independent component analysis classification of laser induced breakdown spectroscopy spectra, *Spectrochim. Acta Part B*, *86*, 31–41.
- Forni, O., et al. (2014), First fluorine detection on Mars with ChemCam on board MSL, 45th *Lunar Planet. Sci. Conf.*, Houston, abstract 1328.
- Fowler A. C., and X. S. Yang (2003), Dissolution/precipitation mechanisms for diagenesis in sedimentary basins, *J. Geophys. Res.*, *108*(B10), 2509, doi:10.1029/2002JB002269.
- Gaft, M., L. Nagli, N. Eliezer, Y. Groisman, and O. Forni (2014), Elemental analysis of halogens using molecular emission by laser-induced breakdown spectroscopy in air, *Spectrochim. Acta B*, *98*, 1–86.
- Garzanti, E., G. Vezzoli, S. Ando, J. Lavé, M. Attal, C. France-Lanord, and P. DeCelles (2007), Quantifying sand provenance and erosion, *Earth Planet. Sci. Lett.*, *258*, 500–515.
- Grant, J. A., and S. A. Wilson (2011), Late alluvial fan formation in southern Margaritifer Terra, Mars, *Geophys. Res. Lett.*, *38*, L08201, doi:10.1029/2011GL046844.
- Grant, J. A., S. A. Wilson, N. Mangold, F. Calef, and J. Grotzinger (2014), The timing of alluvial activity in Gale Crater, Mars, *Geophys. Res. Lett.*, *41*, 1142–1148, doi:10.1002/2013GL058909.
- Grotzinger J. P., et al. (2014), *A Habitable Fluvio-Lacustrine Environment at Yellowknife Bay*, Gale Crater, Mars, *Science*, *343*, doi:10.1126/science.1242777.
- Hauber, E., T. Platz, D. Reiss, L. Le Deit, M. G. Kleinhans, W. A. Marra, T. de Haas, and P. Carbonneau (2013), Asynchronous formation of Hesperian and Amazonian-aged deltas on Mars and implications for climate, *J. Geophys. Res. Planets*, *118*, 1529–1544, doi:10.1002/jgre.20107.
- Hyvärinen, A., J. Karhunen, and E. Oja (2001), *Independent Component Analysis*, 480 pp., Wiley, New York.
- Lasue, J., et al., (2013), *ChemCam Analysis of Martian Fine Dust*, vol. 8, EPSC, London, abstract EPSC2013-867.
- Le Deit, L., E. Hauber, F. Fueten, M. Pondrelli, A. P. Rossi, and R. Jaumann (2013), Sequence of infilling events in Gale crater, Mars: Results from morphology, stratigraphy, and mineralogy, *J. Geophys. Res. Planets.*, *118*, 2439–2473, doi:10.1002/2012JE004322.
- Le Deit, L., et al. (2015), The Potassic sedimentary rocks in Gale crater, Mars as seen by ChemCam onboard Curiosity, 45th Lunar and Planetary Science Conference, Houston, Tex.
- Le Mouéléc, S., et al. (2014), ChemCam remote micro-imager at Gale crater: Review of the first year of operations on Mars, *Icarus*, *249*, 93–107, doi:10.1016/j.icarus.2014.05.030.
- Lerbekmo, J. F., and F. A. Campbell (1969), Distribution, composition, and source of the White River Ash, Yukon Territory, *Can. J. Earth Sci.*, *6*(1), 109–116.
- Léveillé, R. J., et al. (2014), Chemistry of fracture-filling raised ridges in Yellowknife Bay, Gale Crater: Window into past aqueous activity and habitability on Mars, *J. Geophys. Res. Planets*, *119*, 2398–2415, doi:10.1002/2014JE004620.
- Malin, M. C., et al. (2010), The Mars Science Laboratory (MSL) mast-mounted cameras (Mastcams) flight instruments. 41th *Lunar Planet. Sci. Conf.*, abstract 1123.
- Mangold, N., and V. Ansan (2006), Detailed study of an hydrological system of valleys, a delta and lakes in Thaumasia region, Mars, *Icarus*, *180*, 75–87.
- Mangold, N., S. Adeli, S. Conway, V. Ansan, and B. Langlais (2012a), A chronology of early Mars climatic evolution from impact crater degradation, *J. Geophys. Res.*, *117*, E04003, doi:10.1029/2011JE004005.
- Mangold, N., J. Carter, F. Poulet, E. Dehouck, V. Ansan, and D. Lezeau (2012b), Late Hesperian aqueous alteration at Majuro crater, Mars, *Planet. Space Sci.*, *72*, 18–30, doi:10.1016/j.pss.2012.03.014.
- Mangold, N., E. S. Kite, M. Kleinhans, H. Newsom, V. Ansan, E. Hauber, E. Kraal, C. Quantin-Nataf, and K. Tanaka (2012c), The origin and timing of fluvial activity at the Eberswalde crater, Mars, *Icarus*, *220*(2), 530–551.
- Maurice, S., et al. (2012), The ChemCam instrument suite on the Mars Science Laboratory (MSL) rover: Science objectives and mast unit description, *Space Sci. Rev.*, *170*, 95–166, doi:10.1007/s11214-012-9912-2.
- McLennan, S. M., et al. (2014), Elemental geochemistry of sedimentary rocks in Yellowknife Bay, Gale crater Mars, *Science*, *343*, doi:10.1126/science.1244734.

- Meslin, P.-Y., et al. (2013), Soil diversity and hydration as observed by ChemCam at Gale crater, Mars, *Science*, *341*, doi:10.1126/science.1238670.
- Moore, J. M., and A. D. Howard (2005), Large alluvial fans on Mars, *J. Geophys. Res.*, *110*, E04005, doi:10.1029/2004JE002352.
- Nachon, M., et al. (2014), Calcium sulfate veins characterized by the ChemCam instrument at Gale crater, *J. Geophys. Res. Planets*, *119*, 1991–2016, doi:10.1002/2013JE004588.
- Newsom, H. E., et al. (2014), Gale crater and impact processes—Curiosity's first 364 sols on Mars, *Icarus*, *249*, 108–128, doi:10.1016/j.icarus.2014.10.013.
- Ollila, A. O., et al. (2013), Trace element geochemistry (Li, Ba, Sr, and Rb) using Curiosity's ChemCam: Early results for Gale crater from Bradbury Landing Site to Rocknest, *J. Geophys. Res. Planets*, *119*, 255–285, doi:10.1002/2013JE004517.
- Palucis, M., W. Dietrich, A. Hayes, R. Williams, S. Gupta, N. Mangold, H. E. Newsom, C. Hardgrove, F. Calef, and D. Sumner (2014), The origin and evolution of the Peace Vallis fan system that drains to the Curiosity landing area, Gale crater, Mars, *J. Geophys. Res. Planets*, *119*, 705–728, doi:10.1002/2013JE004583.
- Quantin, C., P. Allemand, N. Mangold, G. Dromart, and C. Delacourt (2005), Fluvial and lacustrine activity on layered deposits in Melas Chasma, Valles Marineris, Mars, *J. Geophys. Res.*, *110*, E12S19, doi:10.1029/2005JE002440.
- Sautter, V., et al. (2013a), Igneous mineralogy at Bradbury rise: The first ChemCam campaign, *J. Geophys. Res. Planets*, *119*, 30–46, doi:10.1002/2013JE004472.
- Sautter, V., et al. (2013b), Is Bathurst inlet rock an evidence of explosive volcanism in the Rocknest area of Gale crater? 44th Lunar and Planetary Science Conference, held March 18–22, 2013 in The Woodlands, Texas. LPI Contribution No. 1719, p. 1985.
- Schmidt, M. E., et al. (2014), Geochemical diversity in first rocks examined by the Curiosity rover in Gale crater: Evidence for and significance of an alkali and volatile-rich igneous source, *J. Geophys. Res. Planets*, *119*, 1–18, doi:10.1002/2013JE004481.
- Schröder, S., et al. (2014), Hydrogen detection with ChemCam spectra at Gale Crater, Mars, *Icarus*, doi:10.1016/j.icarus.2014.08.029.
- Sobron, P., A. Wang, and F. Sobron (2012), Extraction of compositional and hydration information of sulfates from laser-induced plasma spectra recorded under Mars atmospheric conditions—Implications for ChemCam investigations on Curiosity rover, *Spectrochim. Acta Part B*, *68*, 1–16.
- Stack, K. M., et al. (2014), Diagenetic origin of nodules in the Sheepbed member, Yellowknife Bay formation, Gale crater, Mars, *J. Geophys. Res. Planets*, *119*, 1637–1664, doi:10.1002/2014JE004617.
- Sumner, D. Y., et al. (2013), Preliminary geological map of the Peace Vallis fan integrated with in situ mosaics from the Curiosity rover, Gale crater, Mars, 44th Lunar and Planetary Science Conference, The Woodlands, Texas. LPI Contribution No. 1719, p. 1699.
- Taylor, S. R., and S. M. McLennan (2009), *Planetary Crusts: Their Composition, Origin, and Evolution*, 378 pp., Cambridge Univ. Press, Cambridge, U. K.
- Vaniman, D. T., et al. (2014), Mineralogy of a mudstone at Yellowknife Bay, Gale crater, Mars, *Science*, *343*, doi:10.1126/science.1243480.
- Wiens, R. C., et al. (2012), The ChemCam instrument suite on the Mars Science Laboratory (MSL) rover: Body unit and combined system tests, *Space Sci. Rev.*, *170*, 167–227, doi:10.1007/s11214-012-9902-4.
- Wiens, R. C., et al. (2013), Pre-flight calibration and initial data processing for the ChemCam laser-induced breakdown spectroscopy instrument on the Mars Science Laboratory rover, *Spectrochim. Acta B*, *82*, 1–27.
- Williams, R. M. E., et al. (2013), Martian fluvial conglomerates at Gale crater, *Science*, *340*, 1068–1072, doi:10.1126/science.1237317.
- Yingst, R. A., et al. (2013), Characteristics of pebble and cobble-sized clasts along the Curiosity rover traverse from Bradbury Landing to Rocknest, *J. Geophys. Res. Planets*, *118*, 2361–2380, doi:10.1002/2013JE004435.